Spring 2022

Characterization of cermet fuel for nuclear thermal propulsion (NTP)

James Floyd Mudd

CHARACTERIZATION OF CERMET FUEL FOR NUCLEAR THERMAL PROPULSION (NTP)

by

JAMES FLOYD MUDD

A THESIS

Presented to the Graduate Faculty of the

MISSOURI UNIVERSITY OF SCIENCE AND TECHNOLOGY

In Partial Fulfillment of the Requirements for the Degree

MASTER OF SCIENCE IN NUCLEAR ENGINEERING

2022

Approved by:

Joseph Graham, Advisor
William Fahrenholtz
Gregory Hilmas

ABSTRACT

A manned flight to Mars is met with many technical challenges, not the least of which is the development of propulsion technology capable of moving a transit vehicle from Earth orbit to Mars orbit. NASA is investigating Nuclear Thermal Propulsion (NTP) as a way of reducing flight time and providing the option for a mid-mission abort. NTP, which uses a high temperature nuclear reactor to heat a propellant, requires advanced fuel materials capable of withstanding temperatures well in excess of 2000 K. Among the fuel options are ceramic metal (cermet) composites composed of refractory metals and Ultra-High Temperature Ceramics (UHTCs).

The mechanical and thermal properties of MoW-HfN, a surrogate cermet for MoW-UN, were characterized over a wide range of elevated temperatures. Thermal diffusivity, the coefficient of thermal expansion (CTE), elastic modulus, and heat capacity were measured. Optical and scanning electron microscopy (SEM) were performed to characterize the microstructure and draw structure-property correlations. The thermal diffusivity was obtained though the laser flash method. Values ranged from about 0.18 cm^2/s at room temperature and decreased down to 0.15 cm^2/s at 1800 °C. The CTE was measured using push rod dilatometry up to 1600 °C, giving average values from 6.0-9.0$\times 10^{-6}$ K^{-1}. Four-point bend tests were conducted from 25-1600 °C revealing systematic strengthening with temperature up to about 1400 °C where strength began to decrease, likely due to the increased ductility of the MoW matrix. A scientific rationalization of the effective material properties is made using the rule-of-mixtures and other effective properties models.

ACKNOWLEDGMENTS

I would like to acknowledge Brian Taylor, Dr. Ryan Wilkerson, Dr. Jhonathan Rosales, and Marvin Barnes of the Marshall Space Flight Center for their input on various aspects in the testing and measurements and the production the MoW-HfN billets. I would also like to acknowledge my advisor Dr. Joseph Graham for his guidance and input with results analysis, Dr. Gregory Hilmas and Dr. William Fahrenholtz for their advice and insight into measurements obtained, and Dr. Jeremy Watts, Dr. Eric Bohannan, Jecee Jarman, and Paul Brune, for their input and training on the various instruments used to prepare and characterize the specimens.

TABLE OF CONTENTS

Page

LIST OF ILLUSTRATIONS

Page

LIST OF TABLES

Page

NOMENCLATURE

Symbol	Description
NTP	Nuclear Thermal Propulsion
UHTC	Ultra High Temperature Ceramic
CTE	Coefficent of Thermal Expansion
SEM	Scanning Electron Microscope
HIP	Hot Isostatic Pressing
SPS	Spark Plasma Sintering
SOFC	Solid Oxide Fuel Cell
LANL	Los Alamos National Laboratory
LLNL	Lawrence Livermore National Laboratory
AEC	Atomic Energy Commission
GE	General Electric Company
bcc	Body Centered Cubic
$\sigma_{a,tot}$	Total absorption cross-section
f_i	Isotope Abundance
$\sigma_{a,i}$	Isotope absorption cross-section
fcc	Face-centered Cubic
P_c	Effective Cermet Property
P_r	Filler Property
P_m	Matrix Property
f	Filler volume fraction

k_r	Thermal conductivity of filler particle
k_m	Thermal conductivity of matrix
k_m	Effective Thermal conductivity of cermet
h_c	Boundary Conductivity
a	Particle Radius
EDM	Electrical Discharge Machining
CAD	Computer Aided Design
$t_{1/2}$	Half Rise Time
L	Sample Thickness
α	Thermal Diffusivity
l_0	Initial Length
Δl	Change in length
ΔT	Change in Temperature
E	Modulus of Elasticit
P	Applied Load
δ_c	Beam Deflection
I	Moment of Inertia
L	Support Span
D	Edge Span
b	Width of beam
h	Depth of Beam

m	Slope of Load vs Deflection curve
σ	Stress
EDS	Energy Dispersive Spectrometer

1. INTRODUCTION

NASA's Nuclear Thermal Propulsion (NTP) program has been tasked with developing and designing nuclear propulsion systems capable of sending manned vehicles to Mars. This comes with a variety of design challenges, a major concern being transit time. The propulsion system needs to rapidly transport astronauts from Earth's orbit to Mars and back. At the same time, this needs to happen efficiently with a minimum fuel weight.

Two properties used to describe propulsion systems are thrust and specific impulse. Thrust is the force that moves a rocket, while specific impulse is a measurement of how efficiently a given mass of propellant is at producing thrust. Conventional propulsion technologies, such as chemical propellants and electrical thrusters, each have strengths and weaknesses in terms of these two properties. Figure 1.1 below gives typical ranges of thrust and specific impulse for different propulsion technologies [1]. Chemical propellants produce high thrust making them suitable for lift vehicles. Their specific impulse, however, is low, meaning that they quickly and inefficiently expel propellant over a short burn time. Electric thrusters, on the other hand, have a high specific impulse, allowing them to eject propellant efficiently over a long burn time. Electric thrusters, however, produce low thrust, meaning that they can only accelerate a payload slowly. While electric thrusters are a suitable option for unmanned spacecrafts where the payload can be designed to withstand a long journey in space, for manned space missions, a short mission time necessary to reduce astronauts' exposure to cosmic radiation, solar storms [2], and zero gravity.

NTP offers a compromise between thrust and specific impulse. Figure 1.2 illustrates a basic NTP system. A liquid propellant, usually liquid hydrogen, is pumped through a nuclear reactor core. As the propellant travels through the core, it is heated and expelled out of a nozzle as a high velocity gas, and thereby produces thrust. Early prototype thrusters developed during the ROVER/NERVA program demonstrated that exhaust velocities and temperatures of 8.1 km s^{-1} and 2700 K, respectively, are possible [3]. The moderate thrust and specific impulse allow for a shorter transit time and ability to perform mid-mission abort [1].

In the evolution of NTP systems, several fuel types have been considered. Historically, cermet fuels have been the main candidate fuel. NASA is currently considering both cermet and cercer (ceramic-ceramic) composite fuels. For this work, a surrogate of high assay low enriched (HALEU) MoW-UN cermet fuel is considered. HALEU is defined as uranium with U-235 concentrations between 5 and 20% [4].

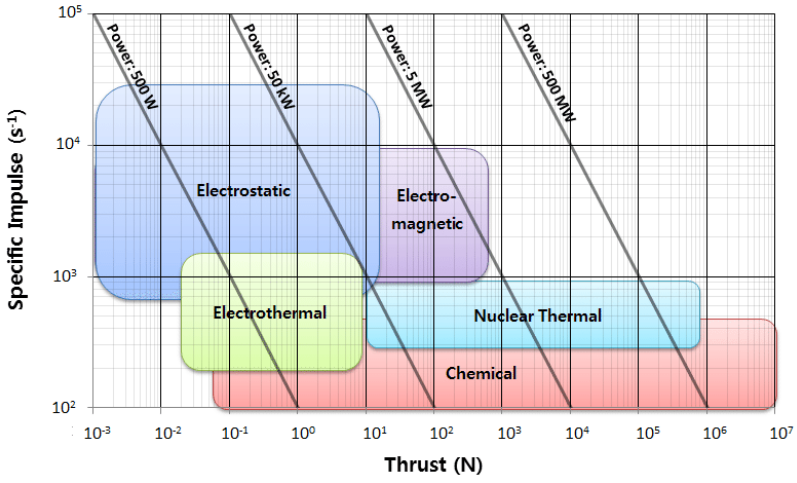

Figure 1.1 Comparison of different conventional propulsion systems [1]

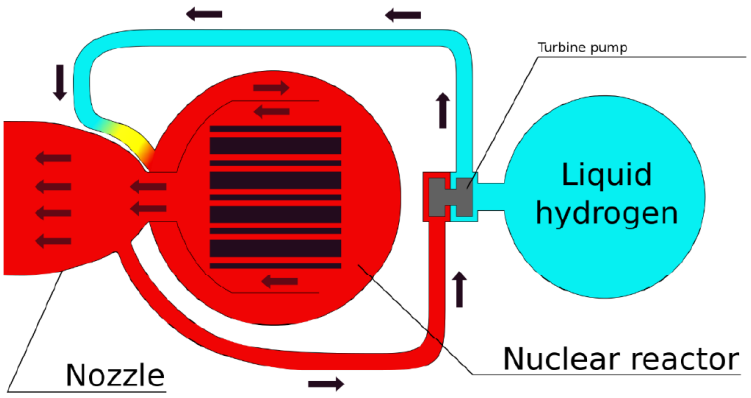

Figure 1.2 A simplified schematic of a NTP system [1]

During a burn, the fuel is exposed to extreme conditions such as temperatures up to ~2850 K, flowing hydrogen propellent, thermal stresses, and high energy ionizing radiation. The reactor and fuel materials must be selected and designed to tolerate these extreme conditions. In addition, constraints on the size and weight of the reactor and transit vehicle are imposed by the lift vehicle used to lift the transit vehicle into Low Earth Orbit (LEO). The size/weight constraints and the use of low enriched uranium requires the use of a fuel with high uranium density.

Given the above constraints, the baseline fuel, MoW-UN cermet, was chosen. The UN ceramic component provides hardness, a high melting temperature (3120 K), and a high uranium density. Considering thermomechanical properties alone, the refractory metal, W, is an desirable metal binder. It provides a high melting temperature (3695 K), high temperature strength and toughness, and resistance to hydrogen corrosion. Mo, though less refractory than W (melting temperature of 2896 K) has a lower neutron absorption cross section than W. When alloyed in a 70/30 ratio, Mo and W, represent a

compromise between high temperature strength, toughness, neutron transparency, and radiation tolerance well suited for use in NTP [5].

Limited data are available on the physical properties of the UN-MoW cermet. The effective properties have been estimated by extrapolating data from similar materials or by employing a variety of effective models. This may be a reasonable approach for properties such as the specific heat capacity where a rule-of-mixtures approach is likely accurate, but it can be difficult to accurately implement for properties that are dependent on transport phenomena or interacting stress fields [5]. In any case, experimental validation is still needed to give reactor modelers confidence that their constitutive materials models are realistic and correctly describe the performance of fuel and reactor under operating conditions. This thesis investigates the high temperature mechanical and thermal properties of the surrogate material MoW-HfN.

2. LITERATURE REVIEW

2.1. CERMETS AND GENERAL PROPERTIES

2.1.1. Overview of Cermets. Cermets are a class of metal-matrix composite (MMC) materials composed of a ceramic phase distributed within a metal matrix/binder (see Figure 2.1). As with other composites, the fundamental benefit of cermets is that they combine the properties and performance of complementary classes of materials. For example, cermets combine the strength and hardness of ceramics with the ductility and toughness of metals, such as shown below in Figure 2.2 [6]. The metal binder also provides cermets with electrical conductivity [7, 8], impact resistance, and thermal shock resistance [9, 10]. Other properties such as corrosion resistance, strength-to-weight ratio, creep resistance can be controlled through the selection of the specific metal and ceramic components.

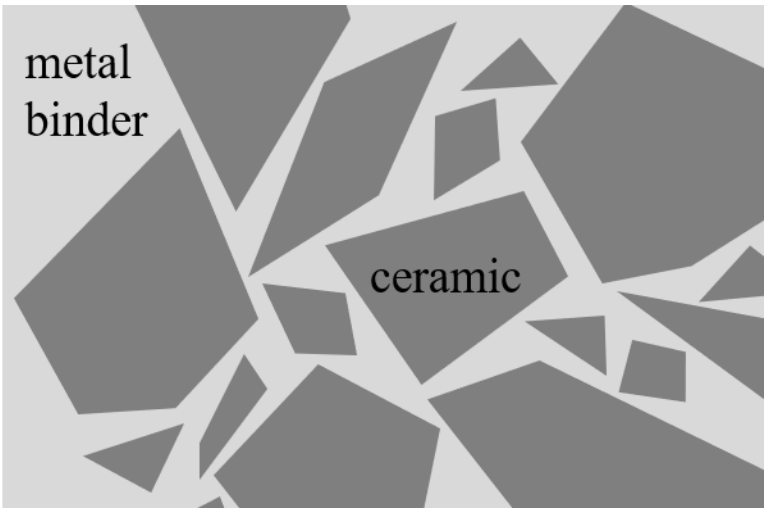

Figure 2.1. Basic cermet microstructure.

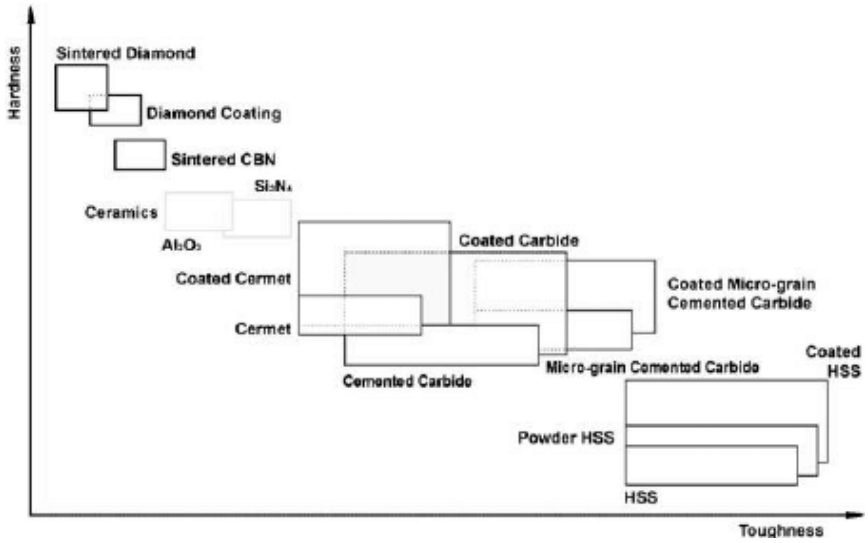

Figure 2.2. Hardness vs. toughness chart of various metals, ceramics and cermets [6].

The definition of cermet is somewhat inconsistent across the literature but is generally restricted to sub-mm particle-reinforced MMCs (though some sources also differentiate MMCs from cermets based on binder fraction). Similarities also exist between cermets and some ceramic fiber reinforced metals though fiber reinforced metals are less frequently referred to as cermets. Cermets containing WC are often referred to as cemented carbides though other carbide based cermets are usually not. Cermets are usually distinguished from dispersion strengthened alloys based on their ceramic volume fraction, with the ceramic phase constituting somewhere between 15-85% of the volume [11].

Besides the properties of the constituent metal and ceramic components, factors that affect a composite's effective properties are particle size, shape, orientation, volume fraction, wettability of metal on ceramic, and solubility of metal in ceramic [12, 13]. The cermet's effective properties can, therefore, be tailored through the choice of the ceramic

metal pair, particle size/shape, and binder fraction. For example, Figure 2.3 shows some effects of particle size and binder fraction on the mechanical properties of WC-Co cermets.

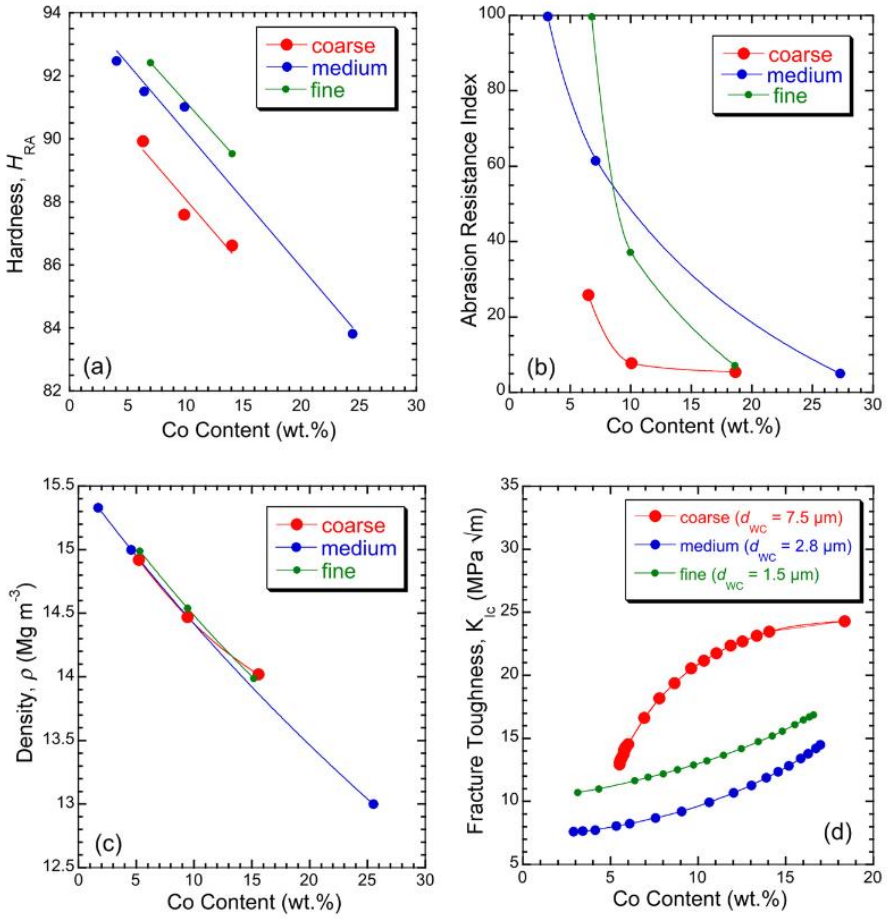

Figure 2.3. Dependence on binder fraction on several material properties for WC-Co cermets [14].

2.1.2. Processing of Cermets. Cermets can be produced though a wide variety of powder metallurgy processing techniques [13]. The usual process for powder metallurgy involves mixing powders of the constituent materials, then consolidation and sintering them through techniques such hot pressing, hot isostatic pressing (HIP), or spark plasma

sintering (SPS) [13, 15, 16, 17]. In hot pressing and HIP, a powder sample is heated and pressure is applied either uniaxially by a ram (hot pressing) or isostatically by a high pressure gas (HIP) to consolidate and densify the powder. SPS is similar to hot pressing, except that heating is accomplished by applying a current through the sample. This allows for more rapid heating of the sample compared to hot pressing, reducing hold times and limiting grain growth [15]. A generalized flowchart showing these and other processing routes are shown in Figure 2.4.

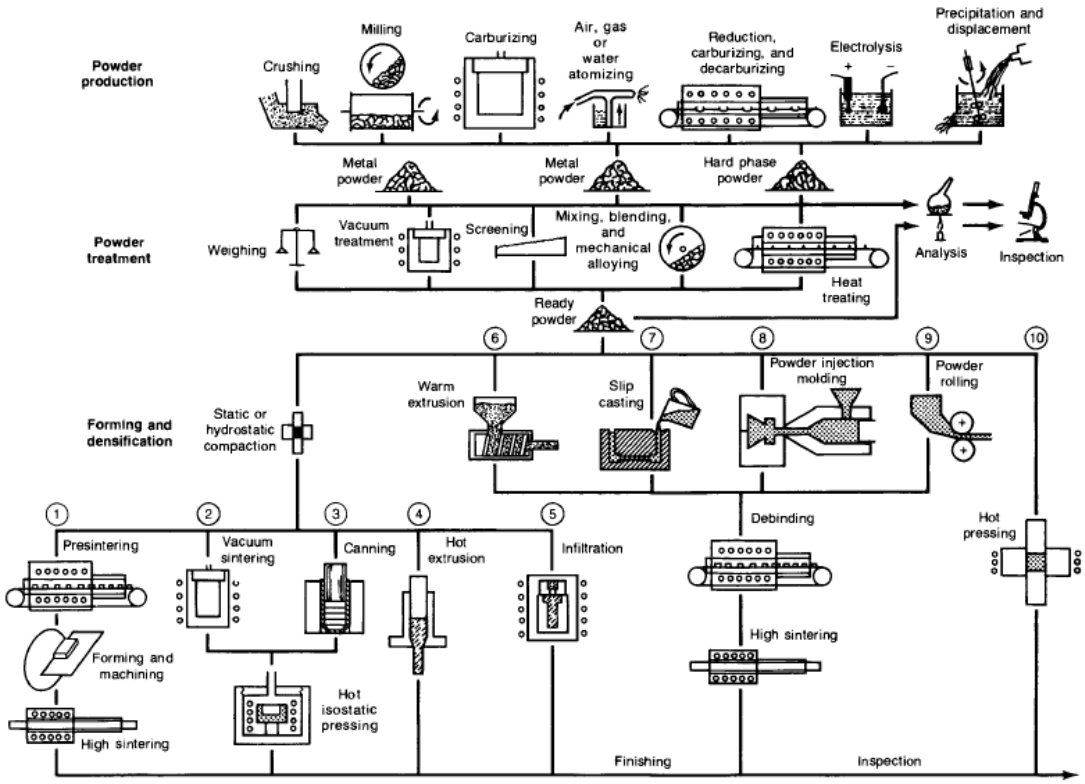

Production method	Products
1. Presintering	Cemented-carbide parts and cermets
2. Vacuum sintering	Steel-bonded carbides (standard pieces) and cermets
3. Canning	Steel-bonded carbides (special pieces)
4. Hot extrusion	Aluminum cermets with moderate amounts of hard-phase additions
5. Infiltration	TiC parts with nickel- or cobalt-base infiltrants and other cermets with about 55–85 vol% hard phase
6. Warm extrusion	Cemented-carbide rods or other slender cermet parts
7. Slip casting	Cermets with high proportions of hard phase
8. Powder injection molding	A wide variety of cermet compositions
9. Powder rolling	Aluminum, copper, and other nonferrous metals with moderate additions of hard-phase components
10. Hot pressing	A wide variety of cermet compositions

Figure 2.4. Flowchart detailing various production techniques for cermets [13].

2.1.3. Use of Cermets. A wide variety of cermets are used in industry today. WC based cermets, especially WC-Co, is widely used for cutting tools in machining applications [18, 19]. Other common cermets for machining applications include TiC-metal and TiN-metal (e.g. metal = Ni, Mo, Co, Al). The wear resistance, hardness, and thermal conductivity of these cermets allow for the cutting tool to preserve its cutting edge [13]. Other cermets based on different carbides (e.g. SiC, Cr_3C_2), oxides (Al_2O_3, SiO_2), and borides (e.g. ZrB_2) have been used in applications where enhanced corrosion and erosion resistance is required [14].

Other oxides, carbides, and nitrides have been used in more specialized systems. For example, nickel-yttria stabilized zirconia (Ni-YSZ) is used as an anode in solid oxide fuel cells (SOFCs) [20]. SOFC are devices that create an electric current by oxidizing a fuel, typically hydrogen or hydrocarbons, on an anode material. They are typically operated at temperatures around ~900-1000 °C to permit use of a wider range of fuels and to increase the reaction rate [22, 23]. Since liberated electrons enter the anode surface, the anode must be electrically conductive and have a coefficient of thermal expansion (CTE) similar to the electrolyte to minimize thermal stresses arising from CTE mismatch. Porous Ni-YSZ cermets have been developed which meet these requirements for the anode. The interconnected Ni phase acts as a pathway for electron transport, while the YSZ provides ionic conductivity and helps with CTE compatibility with the electrolyte [24].

In nuclear energy, cermets have been utilized in reactor fuels. Compared to conventional oxide fuels (UO_2, PuO_2, ThO_2) cermets have higher thermal conductivity which is advantageous in terms of heat transfer and safety margins for melting. Other

properties that make cermets desirable is their ability to withstand thermal shock, which the fuel can experience in reactors that require rapid power changes [21], retention of fission products, and, in the case of refractory metal-based cermets, high operating temperatures [15, 16, 21]. Although no commercial nuclear power plants currently utilize cermet fuels, UO_2-stainless steel is employed in U.S. military reactors, while UO_2 dispersed in an Al-Zr matrix is used in some research reactor fuels [21]. U_3Si_2-Al dispersion fuel is also used in some research reactors could also be considered a cermet.

The development of refractory metal-based cermet nuclear fuel has largely been driven by the United States' efforts to develop Nuclear Thermal Propulsion (NTP) systems. As this work relates to cermet fuel for NTP systems, that topic is discussed in greater detail in the following sections.

2.2. CERMETS USED IN NUCLEAR THERMAL PROPULSION

2.2.1. Historical Development & Material Requirements of NTP. The U.S. officially began its research into nuclear thermal propulsion technology in 1955 at Los Alamos National Laboratory (LANL) and Lawrence Livermore National Laboratory (LLNL) [2, 25]. One of the main programs that arose from this was the ROVER/NERVA project. The goal of that project was to develop experimental nuclear thermal propulsion reactors managed jointly by NASA and the Atomic Energy Commission (AEC) [2]. This program, in turn, was split into four main projects: KIWI, NERVA, PHOEBUS and RIFT. A flow chart of the ROVER project can be seen in Figure 2.5, summarizing the relations between each project and their respective timelines [2].

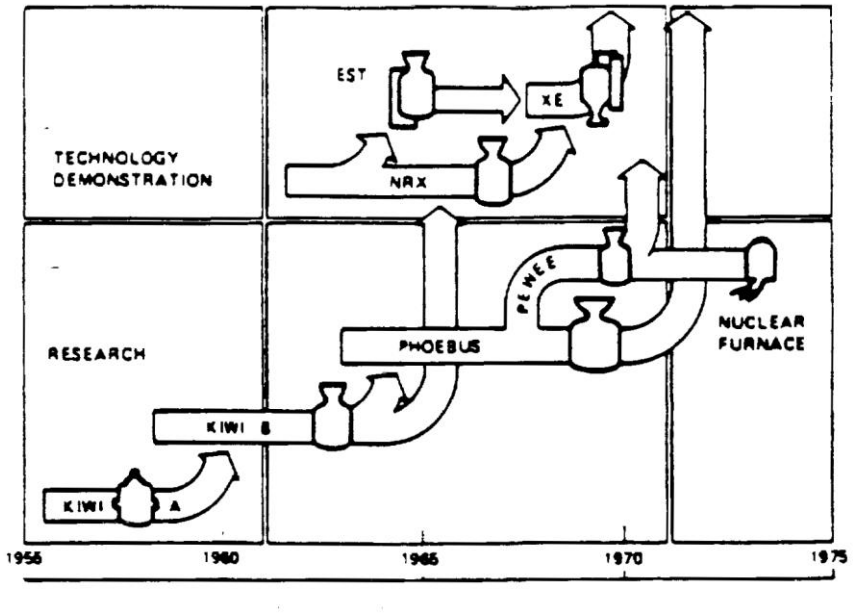

Figure 2.5. A flowchart summarizing the test programs of the ROVER project [2].

The KIWI project was a series of terrestrial nuclear reactors used to collect experimental reactor data and develop testing procedures [26]. KIWI-A was a MWt design used to: demonstrate that a high-power density reactor could heat a gaseous hydrogen propellant to high temperatures in a quick and stable manner; establish basic testing procedures; and study the graphite-hydrogen interaction [2, 26]. Later iterations, KIWI-A' and KIWI-A3, improved upon each of the previous reactor designs, and collected data related to the temperature coefficient of reactivity of the core, core response to sudden changes in flow and/or power, and structural integrity of the core. KIWI-B series reactors were 1000 MWt reactors that used liquid hydrogen as opposed to gaseous hydrogen [2, 26]. PHOEBUS was a project running parallel to KIWI, which aimed to build reactors with higher powers and longer operating times.

The NERVA project focused on developing the first generation of nuclear rocket engines based on designs from the KIWI project. The main objective was to create an engine capable of producing 245 kN of thrust and a specific impulse of 7450 m s^{-1} at a power level of 1100 MWt [2, 26]. It consisted of the reactor series NRX, XE, and EST, which each addressed the different objectives of the NERVA project. NRX and EST eventually lead to the final development of the XE' reactor, which was the first downward firing prototype, capable of producing a thrust of 247 kN and specific impulse of 7000 m s^{-1} at 1140 MWt meeting the overall goal of the program [2, 26].

RIFT was solely headed by NASA, unlike the previous projects which were jointly managed by NASA and the AEC. Its main objective was to develop, fabricate and test fly a NERVA vehicle for use as an upper-class stage on a Saturn-class launch vehicle [26]. However, after ejection of fuel elements was observed in KIWI B1B and B4A tests, the nuclear rocket program was reassessed, and the RIFT project was cancelled [2, 25, 26].

In selecting fuel materials for NTP system, one tries to maximize a number of performance parameters including fission product retention, melting point, actinide density, radiation stability, and thermal shock resistance [25, 27]. Under these requirements, a number of different cermet fuels have been studied including UO_2 and UN based cermets with W, W-Re or Mo binders [25].

2.2.2. W-UO_2. One of the first fuels to be developed and tested for NTP was a W-UO_2 cermet. These fuels were investigated in the GE-710 program and the Argonne National Laboratory (ANL) Cermet Nuclear Rocket Program. The main objective of these programs was to develop fuels that were able to operate in a high temperature

environment (>2000 °C) for multiple hours in H_2 or inert gas coolants for multiple thermal cycles [25, 27]. W-UO_2 was investigated due to its high temperature stability and hydrogen compatibility [27]. Figure 2.6 shows the fabrication process used by the General Electric Company (GE).

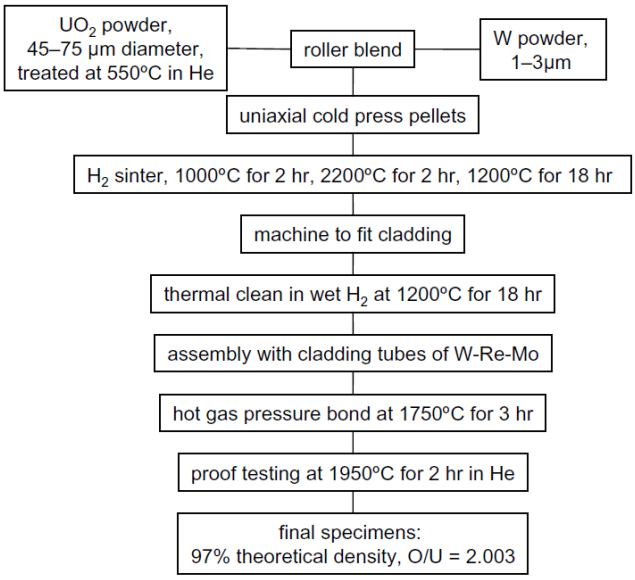

Figure 2.6. Flow chart for W-UO_2 cermet production from General Electric [27].

Thermal testing was performed to measure the mechanical stability for conditions similar to the expected reactor operation. The two primary failure modes identified were loss of fuel and loss of mechanical integrity [27]. Mechanisms that contributed to these failures included formation of metallic U at high temperatures that reacted to form uranium hydride, thermal expansion mismatch between the fuel and metal matrix, and fuel vaporization. Some solutions that addressed these issues were to add stabilizers to

the UO_2, enhance the ductility of the metal matrix by using alloys containing Mo or Re, and add coatings around UO_2 particles to minimize contact between particles. [25, 27]

2.2.3. Alternatives to W-UO_2. Other metals and alloys have been considered alongside W, with the goal of identifying a suitable binder that could improve the mechanical integrity and reduce fuel loss during thermal cycling in hydrogen [27]. UO_2-based cermets using pure Mo, pure Re, and Mo and Re alloys have been studied. In those tests, specimens were heated to ~2000 °C, held at that temperature over the span of several minutes to an hour before cooling down. This process was repeated a number of times [16, 27]. As will be mentioned later, the move to a predominantly Mo based alloy has certain neutronic advantages as well.

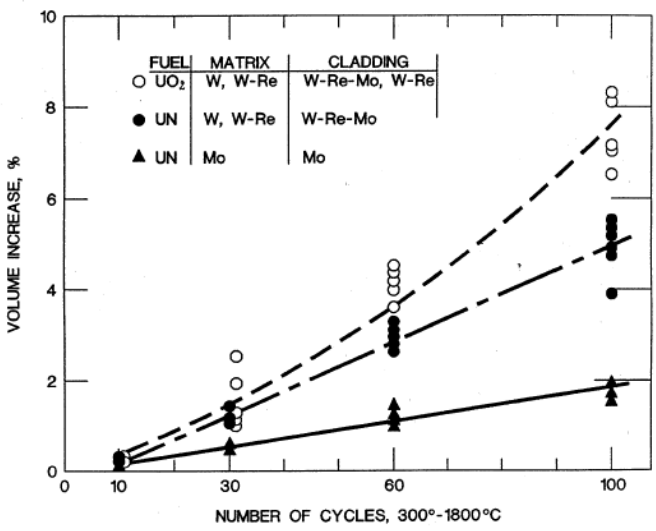

Figure 2.7. Volume increase of different cermet fuels during thermal cycling [25].

Fabrication of alternative fuel types using UN instead of UO_2 were also investigated later in the GE 710 program [27]. UN has several advantages over UO_2. Its

higher U density and lower CTE allow for more compact core design and reduction in volume expansion, which can be seen illustrated in Figure 2.7 [25]. Though some property data was gathered on UN cermets in the GE 710 program, a lack of data on UN cermet fuels still exists [25].

2.2.4. Properties of Mo, W, UN, and HfN. Molybdenum and tungsten form a continuous range of solid solution alloys due to their similar atomic radius and body centered cubic (bcc) structure. Due to the alloy's high melting temperature, ranging from 2625-3410°C, it is considered a refractory metal [12, 28]. The nominal binder studied in this work is a 30 at. %W MoW alloy. However, as the results section will show, due to the use of separate Mo and W powders during processing, the actual binder is a two-part matrix with distinct Mo and W domains. Therefore, the properties of pure Mo and W will also be reviewed.

The mechanical properties of Mo-W alloys have been previously characterized over a wide range of temperatures, as shown in Figure 2.8 [29]. The main mechanism of strengthening that occurs in the alloy is solid solution strengthening. This is due to the strain imposed on the lattice by the substitutional atom, providing resistance to dislocation motion [12, 28]. As the tungsten content increases, the strength of the alloy is also shown to increase [29], shown in Figure 2.8. As the tungsten concentration increases, an increase in both the ultimate and yield strength are seen. Even a modest 20 wt% tungsten addition in molybdenum gives high temperature strength similar to that of pure tungsten.

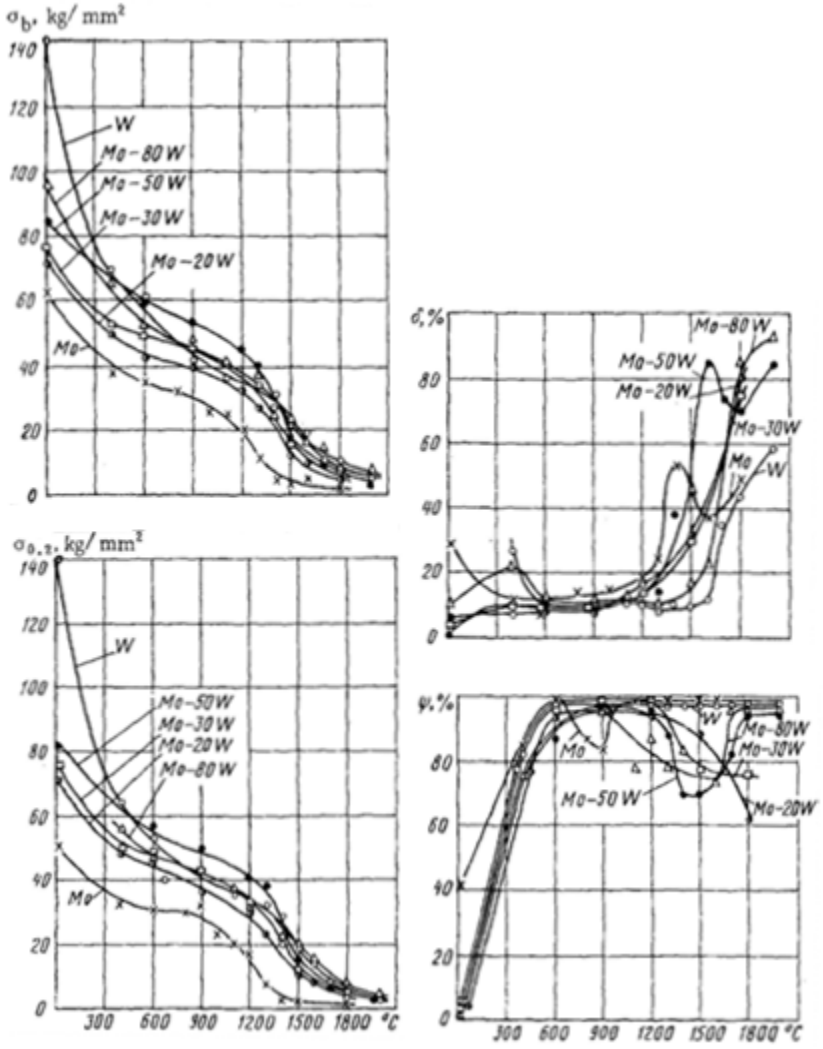

Figure 2.8. Ultimate strength (top left), yield strength (bottom left), percent elongation (top right) and reduction in cross section (bottom right) of MoW alloys and pure Mo and W at various temperatures [29].

Pure tungsten was initially used in cermet fuels in the ROVER/NERVA program due to its stability at high temperatures and compatibility with H_2. However, neutronically speaking, W is not a preferred choice. Due to its lower thermal neutron absorption cross section compared to W, Mo and Mo alloys have been considered more recently as the binder [15, 30]. Table 2.1 shows the thermal neutron absorption cross

section of Mo and W, along with the total absorption cross-section calculated with Equation 2.1 below [31].

$$\sigma_{a,tot} = \sum_i f_i \sigma_{a,i} \qquad \text{Equation 2.1}$$

Where $\sigma_{a,tot}$ is the total absorption cross section, f_i is the abundance, and $\sigma_{a,i}$ is the absorption cross-section of the isotope. The cross-sections and abundances for each isotope can be found in the Appendix. At thermal energies, Mo has a cross section of about 2.7 b, while W has a 18.5 b cross section in the thermal range.

Table 2.1. Microscopic absorption cross-sections for W and Mo [31].

Material	Thermal Absorption Cross Section (b)
Mo	2.51
W	18.26

Use of low enriched uranium (<20 wt% ^{235}U) limits the macroscopic fission cross section of the fuel. In order to achieve criticality, non-fission absorption must be minimized, and uranium density maximized. MoW (30 at% W) represents a compromise between neutronic performance and high temperature strength while UN provides a higher uranium density (13.5 g cm^{-3}) than oxide fuel (9.8 g cm^{-3}) [30, 32].

The room temperature properties of Mo and W can be seen in Table 2.2. Both Mo and W have similar room temperature molar heat capacities, C_p, following the Dulong-Petit law. At elevated temperatures, the electron contribution to the molar heat capacity is greater for Mo [33] and both metals exceed the Dulong-Petit law.

Table 2.2. Physical and thermal properties of Mo and W at room temperature [34]

Element	Density ρ ($g\ cm^{-3}$)	Coefficient of Thermal Expansion $\alpha \times 10^{-6}$ (K^{-1})	Specific Heat C_p $J\ g^{-1}\ K^{-1}$ ($J\ mol^{-1}\ K^{-1}$)	Thermal Conductivity λ ($W\ m^{-1}\ K^{-1}$)
W	19.3	4.5	0.132 (24.27)	174
Mo	10.2	4.8	0.251 (24.06)	138

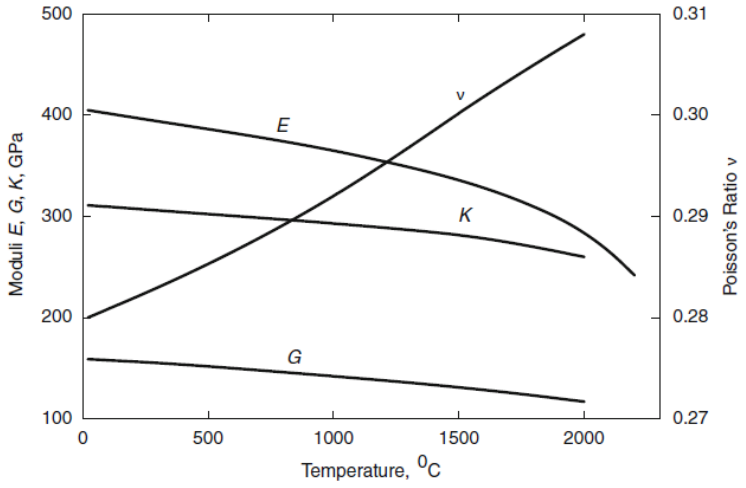

Figure 2.9. Young's, bulk, and shear moduli and Poisson's ratio of pure polycrystalline tungsten [36]

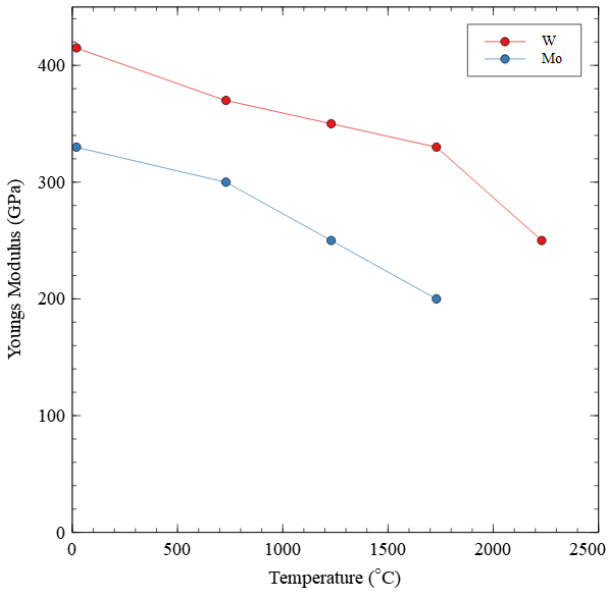

Figure 2.10. Youngs modulus of Mo and W over various temperatures [36].

Figure 2.10 shows the Young's, bulk, and shear moduli of pure polycrystalline tungsten, along with Poisson's ratio over temperatures of 20 to ~2000 °C [35]. At room temperature, the Young's modulus is 400 GPa, and decreases to ~280 GPa at 2000 °C. The Young's modulus of Mo and W are shown in Figure 2.11 [36].

A typical thermal conductivity curve of W is shown in Figure 2.12. The solid line indicates the average value while the arrows indicate the variance in the data from various sources. Transport properties such as the thermal conductivity are influenced by microstructure and crystallinity, hence the large variation in values. As with most metals, the thermal conductivity decreases with temperature due to electron-phonon scattering. A similar trend can be seen for Mo in Figure 2.13.

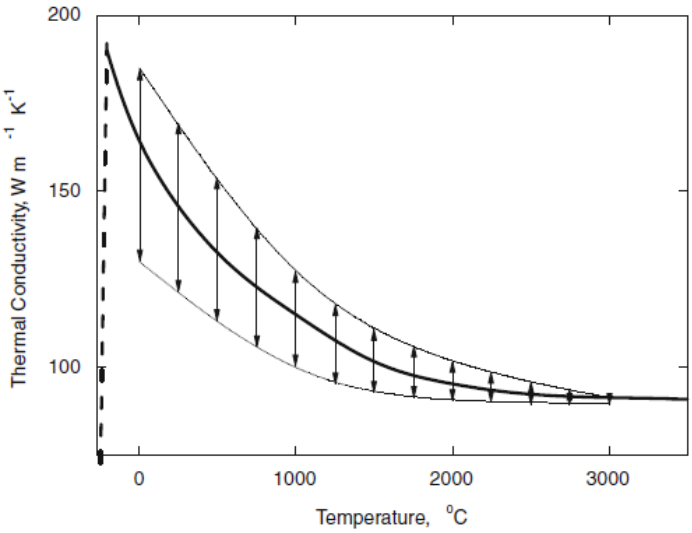

Figure 2.11. Thermal conductivity of tungsten [36]. Arrows indicate spread of data from various sources.

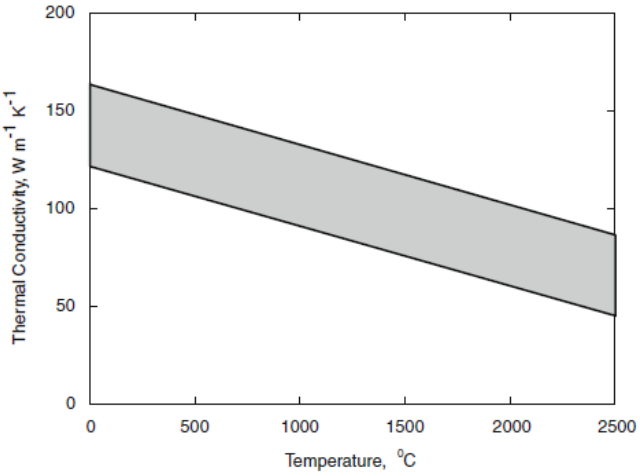

Figure 2.12. Thermal conductivity of Mo over various temperatures [36].

Figure 2.14 gives the linear expansion coefficient of Mo. At room temperature, the expansion coefficient ranges from 5.2-5.5×10^{-6} K^{-1} and increases to 8-10×10^{-6} K^{-1} at 2500 °C [36]. This is slightly higher than the thermal expansion coefficient of W, which

varies from 4-6×10^{-6} K^{-1} at room temperature and increases to 7-11×10^{-6} K^{-1} at 3000°C, increasing almost linearly [36].

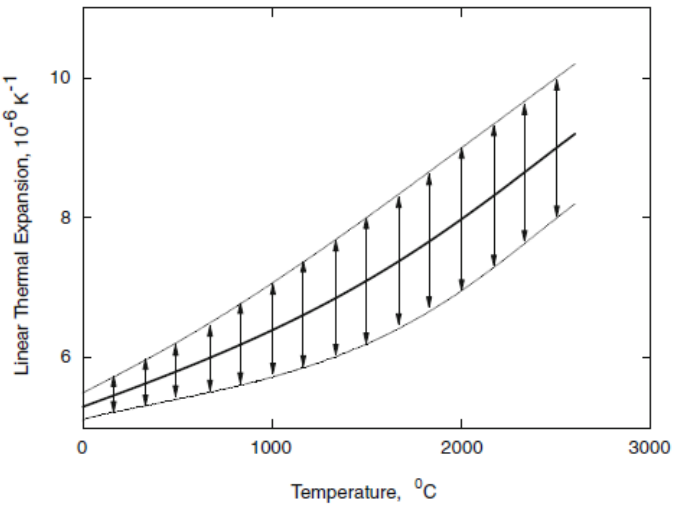

Figure 2.13. Linear expansion coefficient of Mo [36]. Arrows indicate spread of data from various sources.

UN has a 40% higher U density than UO_2 and melting point of 3078 °C [37, 38]. UN also has a higher thermal conductivity than UO_2, as shown below in Figure 2.15.

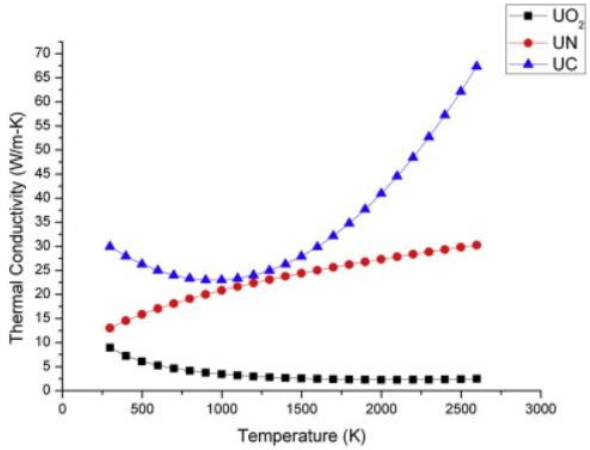

Figure 2.14. Thermal conductivity of UN, UO_2, and UC [35].

At 2000 K, UN has a thermal conductivity of ~25 W m^{-1} K^{-1} while UO_2 is an order of magnitude lower at ~2 W m^{-1} K^{-1}. This higher thermal conductivity allows for lower power peaking and a higher coolant temperature for a given peak fuel temperature [35]. The thermal expansion coefficient of UN can be seen below in Figure 2.16. At 400 °C, UN has a CTE of ~8×10^{-6} K^{-1}, and increases to ~10×10^{-6} K^{-1} at 1600 °C [39]. It has an elastic modulus of 206 GPa at RT [40].

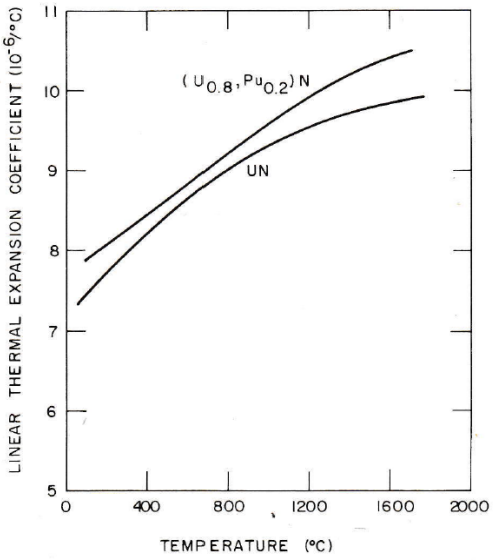

Figure 2.15. Coefficient of thermal expansion of UN and (U,Pu)N [39]

HfN is used as a non-radioactive surrogate material for UN due to its chemical and structural similarity, each material having a face centered cubic (fcc) rock salt structure ($Fm\bar{3}m$ space group) [41, 42, 43]. HfN is classified as an ultra-high temperature ceramic (UHTC). UHTCs are defined as a class of materials which have melting points above 3000 °C. Other properties common to UHTCs are high hardness and strength at room and elevated temperatures [44].

HfN has a melting point of 3385 °C, a density of 13.9 g cm^{-3}, coefficient of thermal expansion (CTE) of 6.9×10^{-6} K^{-1}, a thermal conductivity of 23 W m^{-1} K^{-1}, and a Young's Modulus of 380 GPa at ambient temperatures [45, 46]. Figure 2.17 shows the thermal expansion and conductivity over a range of temperatures.

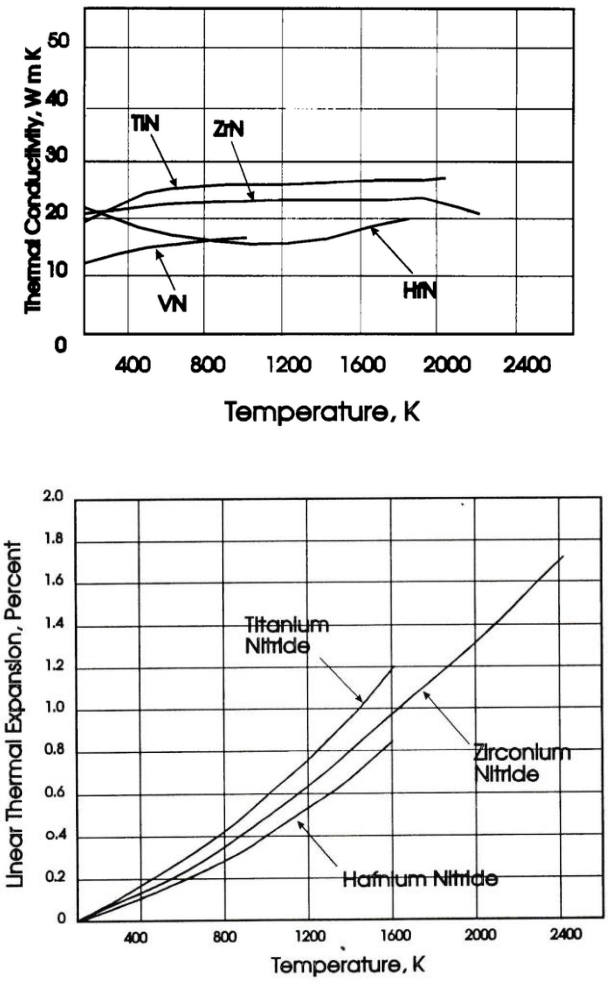

Figure 2.16. The thermal conductivity (top) and total thermal expansion (%) (bottom) of HfN over a wide range of temperatures [45].

2.3. MODELS FOR EFFECTIVE MATERIAL PROPERTIES

In some cases, it is possible to predict the effective properties of a composite given the properties of the constituents. This might be done because experimental property data for the composite do not exist. Effect property models, when valid, also provide the materials engineer with predictive tools for understanding how processing parameters can be tailored to obtain a desired set of material properties.

Different models have been evolved to describe effective properties. The most basic models are the Rule of Mixtures (ROM) and Inverse Rule of Mixtures (IROM), which are described by Equation 2.2 and 2.3, respectively:

$$P_C = fP_r + (1-f)P_m \qquad \text{Equation 2.2}$$

$$\frac{1}{P_C} = \frac{f}{P_r} + \frac{(1-f)}{P_m} \qquad \text{Equation 2.3}$$

P_c is the effective property of the composite, P_r is the property of the reinforcement material (ceramic particle), P_m the property of the matrix material (metal binder), and f is the volume fraction of reinforcement. Both the Rule of Mixtures and Inverse Rule of Mixtures are appropriate for additive properties that are independent of microstructure, such as heat capacity. They can also give order of magnitude estimates for other property values. However, non-additive properties such as thermal conductivity and strength are not necessarily well described by a simple ROM [28, 47].

In a cermet, multiple interfaces exist between particles and binder. When heat flows through those interfaces, a temperature drop occurs. This can be described by thermal resistance which is split into two separate contributions: thermal contact

resistance and thermal boundary resistance [47]. Thermal contact resistance describes the thermal resistance arising from the quality the interface separating phases, while thermal boundary resistance is due to differences in the intrinsic physical properties (i.e. vibrational, chemical bonding) of the constituents.

One of the first models that considered heterogeneous mediums was the Maxwell model. It considers the problem of a dilute dispersion of spherical particles in a continuous matrix but ignores contact resistance between the matrix and particles [47]. The Maxwell model gives an effective thermal conductivity described by Equation 2.4:

$$\frac{k_{eff}}{k_m} = 1 + \frac{3f}{\left(\frac{k_r+2k_m}{k_r-k_m}\right)-f} \qquad \text{Equation 2.4}$$

where k_r is the reinforcement conductivity, k_m is the matrix conductivity, and k_{eff} is the effective conductivity. This model is only valid at lower filler volumes (<25%) since the spacing between particles must be large enough for the assumption of no particle interaction to hold true. Another constraint of this model is that it does not consider the size of the particles. The interfacial resistance becomes more important as particle size decreases (and interfacial area increases). The Hasselman-Johnson model, which builds on the Maxwell model, accounts for the particle size and shape along with the interfacial resistance. Equation 2.5 below

$$k_{eff} = k_m \left(\frac{2\left(\frac{k_r}{k_m} - \frac{k_r}{a*h_c} - 1\right)f + \frac{k_r}{k_m} + \frac{2k_r}{a*h_c} + 2}{\left(1 - \frac{k_r}{k_m} + \frac{k_r}{a*h_c}\right) + \frac{k_r}{k_m} + \frac{2k_r}{a*h_c} + 2} \right) \qquad \text{Equation 2.5}$$

shows the case for a spherical particle, where the h_c is the boundary conductivity and a is the particle radius.

For volume fractions up to 74%, the Bruggeman model is often used. It assumes that a composite can be constructed incrementally by making small changes to the material [5, 47]. Equation 2.6 gives the effective conductivity for the case of mono-sized spheres:

$$k_{eff} = k_r + (1 - f)(k_m - k_r)\left(\frac{k_{eff}}{k_m}\right)^{1/3} \qquad \text{Equation 2.6}$$

This model has been successful at predicting the conductivity at higher filler fractions but must be solved numerically.

3. MATERIALS AND METHODS

3.1. MATERIAL SYNTHESIS AND PROCESSING

The billets used were produced by NASA. Separate powders of Mo, W, and HfN were blended in a Turbula blender mixer for ~1 hour. The W and Mo powders were obtained from Alfa Aesar while HfN was obtained from the Space Nuclear Propulsion Program in NASA. The nitride particle size was sub 45 μm, and the metal powders in single digit micron size. These were then weighed and loaded into graphite dies for hot pressing. They were heated to 1800 ℃ at 100 ℃/min and held for 10 minutes at a pressure of 35 MPa in a He atmosphere. Afterwards, the specimens were allowed to cool freely (initial rate of ~150 ℃/min), and then removed from the dies with a Carver hydraulic press. Multiple billets of MoW-HfN were received for initial testing. The billet composition was 60% vol HfN and 40% vol MoW alloy (30 at% W), measuring at 12 mm thickness and 40 mm diameter.

Table 3.1. Type and number of specimens cut from the billet.

Specimen Type	Dimensions	Number
Laser Flash	Height: 2 mm Diameter: 12.7 mm	6
DSC	Height: 2 mm Diameter: 2 mm	8
Flexure Bar: Type A	1.5 x 2 x 25 mm bars	34
Dilatometry Bars	2 x 2 x 37.5 mm	6

Using wire electrical discharge machining (EDM), a billet was cut into 4 layers of ~2.2 mm thickness. The EDM machine used was an Agie Model #HSS150. The layers were then ground down to 2 mm thickness. In total, 6 laser flash specimens, 6 expansion bars, 8 differential scanning calorimetry (DSC) specimens, and 34 Type A flexure bar specimens were cut to the dimensions specified above in Table 3.1. Type A bars are flexure bars with dimensions of 1.5×2×25 mm. The flexure bars were cut slightly larger than the final dimensions (e.g., 1.8 instead of 1.5 mm) to allow for grinding and polishing of the tensile surfaces to specification. The grinding process was as follows: bars were mounted and ground down to 1.5 mm on each side, then polished down to a 0.25 μm surface finish on one side. Computer Aided Design (CAD) schematics of the specimen dimensions are given in the Appendix.

3.2. TESTING STANDARDS AND PROCEDURES

After the specimens were machined, property characterization began using the following standards for each test. In some cases, the true standard could not be followed, so a modified version was used. The modified procedure followed is outlined when applicable.

3.2.1. Laser Flash Testing. ASTM E1461 was followed to obtain the thermal diffusivity measurements [48]. An Anter Thermal Properties Analyzer (FLASHLINE 5000 Pittsburgh, PA) was used to conduct the laser flash test. In a laser flash measurement, a thin disc at initial temperature T_0 is subjected to an instantaneous pulse of energy which is absorbed in a thin layer on the front face. This causes a temperature rise of ΔT in the rear face, eventually reaching maximum temperature. By knowing the

sample thickness and time to half max temperature, the thermal diffusivity is calculated from solution to the heat equation. A schematic of the process for measuring the thermal diffusivity is shown below in Figure 3.2.

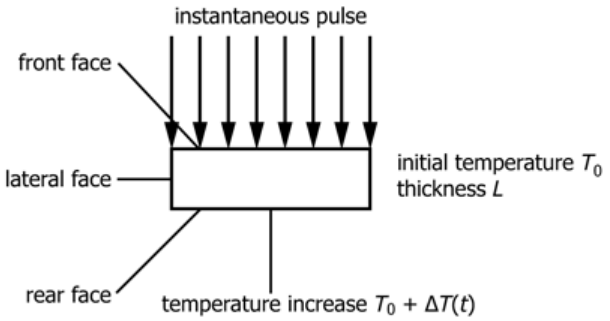

Figure 3.1. A schematic showing the laser flash method [48].

The thin disc specimen, 12.7 mm diameter and 2 mm height in this work, is prepared by applying a thin high emissivity coating to the surface. This is then subjected to a short duration laser pulse, which should be less than 2% of the time it takes the back surface to reach half-max temperature. As specified by the standard, the half-max temperature was reached in 10-1000 ms [48]. The high emissivity is required to allow as much thermal energy to be radiated as infrared light from the rear side. The high emissivity coating (carbon) also improves the absorbance on the front face (laser side). If the absorbance and emissivity are known, the heat capacity and thermal conductivity can also be estimated.

By recording the time required for the rear face to reach half the maximum temperature, known as the half-rise time $t_{1/2}$, and the sample thickness L, the thermal diffusivity α calculated using Equation 3.1 below.

$$\alpha = 0.13879 \frac{L}{t_{1/2}}$$ Equation 3.1

Reliable laser flash measurements were only possible below 600 °C with the carbon coating. Separate experiments conducted using a sacrificial specimen in contact with graphoil in an 800 °C furnace showed that a reaction layer can form at elevated temperatures. Therefore, it was necessary to modify the surface preparation using a method that minimized the surface exposure to carbon while darkening it and improving its emissivity.

To darken the specimens, they were wet etched in a 3% HF solution for approximately 2 hours, then rinsed in deionized water and allowed to dry. A side-by-side comparison of the specimens can be seen below in Figure 3.3, with the etched sample on the left and unetched on the right.

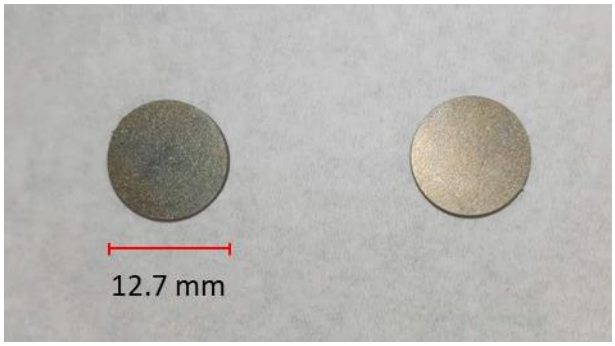

Figure 3.2. Etched (left) vs. unetched thermal diffusivity specimens

The etched surface has unknown emissivity and absorbance. Therefore, the heat capacity and thermal conductivity can no longer be reliably determined with the test method. Diffusivity, which depends only on the half rise-time and sample thickness, can

still be measured. The thermal diffusivity was measured 3 times per temperature, from 200 to 600 °C in 100 °C intervals, and from 600 to 1800 °C in 200 °C intervals. Specimens were heated at a ramp rate of 5 °C/min. Diffusivity was measured along heating and cooling paths to determine if any hysteresis was present in the measurements.

3.2.2. Push Rod Dilatometry. ASTM E228 was followed to obtain the coefficient of thermal expansion [49]. A specimen with length between 25-60 mm and diameter or equivalent diameter between 5 to 10 mm is recommended; however, no limitations exist for either dimension provided the holder containing the specimen has a maximum thermal gradient of 2 °C. A single push rod system works by measuring the change in length of the sample relative to the holder as a function of temperature. By measuring the initial length, the thermal expansion coefficient can be determined by Equation 3.2:

$$CTE = \frac{1}{l_0}\left(\frac{\Delta l}{\Delta T}\right) \qquad \text{Equation 3.2}$$

where CTE is the coefficient of thermal expansion, l_0 is the initial specimen length, and Δl is the change in length for a given change in temperature, ΔT. The ratio of $\Delta l/l_0 \times 100$ is also known as the percent linear change, or PLC. Measurements were obtained from 25 to 1600 °C with a ramp rate of 3 °C/min for 3 separate specimens in an inert Ar atmosphere.

3.2.3. Four-Point Bend Test. ASTM C1161 and ASTM C1211 were used for the ambient and elevated temperature flexure tests, respectively [50, 51]. An Instron 4204 screw-driven test frame with a custom-built environmental chamber and induction

heating system was used to conduct the high temperature flexure test. The standard calculates the flexure stress based on simple beam theory, assuming that: the material is isotropic and homogenous, the modulus of elasticity in tension and compression are similar, and deformation is in the linear elastic regime.

Specimens were prepared as Type A bars, and the tensile surface was polished down to 0.25 μm. A four-point semi-articulating flexure fixture was used to load the specimen. Knowing the applied load, measured deflection, and beam dimensions, the elastic modulus, *E*, can be calculated using Equations 3.3 and 3.4:

$$E = \frac{P}{\delta_c}\frac{D}{48I}(3L^2 - 4D^2) = m\frac{D}{48I}(3L^2 - 4D^2) \quad \text{Equation 3.3}$$

$$I = \frac{h^3 b}{12} \quad \text{Equation 3.4}$$

$$\sigma = \frac{3PD}{h^2 b} \quad \text{Equation 3.5}$$

where *P* is the applied load, δ_c is the beam deflection, *I* is the second moment of inertia, *L* is the support span, *D* is the edge span, *b* is width of beam, *h* is depth of beam, and *m* is the slope of the linear portion of the load-deflection curve. The stress, σ, was also calculated using Equation 3.5 at the maximum load.

Crosshead speeds for the test frame were chosen so that the time to failure was between 10-30 seconds. For the elevated temperature test, it was necessary to test in an inert atmosphere to prevent oxidation of the specimen. Argon gas was used to backfill the test chamber. The crosshead speeds were adjusted for each temperature of interest for failure to fall between 10-30 seconds. Measurements were done for a total of 7

temperatures: room temperature and 800-1600 °C in 200 °C increments. 5 bars were tested at each temperature, except for 1600 °C where 4 bars were tested.

3.2.4. Microscopy and Particle Analysis. Optical images were taken of a polished piece of the HfN-MoW material using a Hirox Digital Microscope. A sample was polished down to a 1 μm abrasive particle size and images were obtained on low magnification. To confirm the composition and phases of the billet, a Helios NanoLab 600 dual beam Scanning Electron Microscope (SEM) with energy dispersive spectrometer (EDS) was used. Using ImageJ, an image analysis software, the particle size distribution of the HfN particles was obtained from the SEM images.

4. RESULTS AND DISCUSSION

4.1. THERMAL EXPANSION

The percent linear change (PLC) was obtained from three separate dilatometry bars over the range of temperatures from 25-1600 °C at a heating rate of 3 °C/min, shown in Figure 4.1. At 1600 °C, the PLC ranges from 1.2-1.6%. The variance may result from variations in the microstructure of the bars due to their different positions they were cut from the billet.

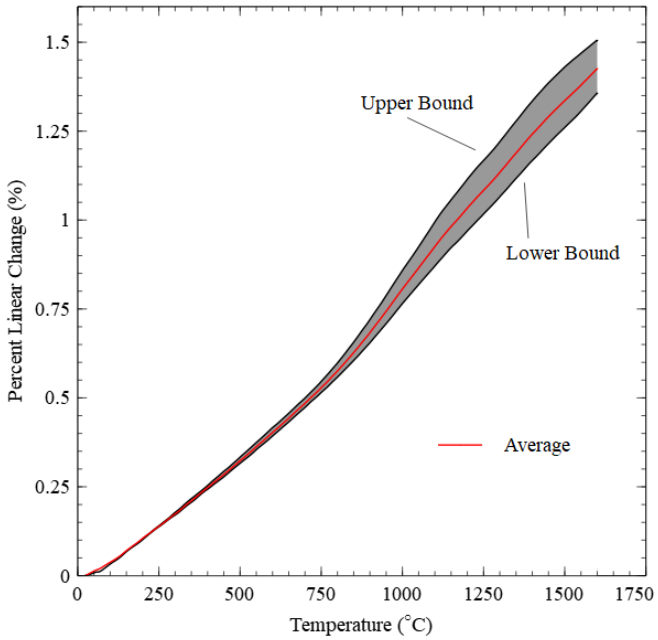

Figure 4.1. Percent Linear Change (PLC) of the expansion bars

The CTE was calculated using Equation 3.2. The CTE curve is shown below in Figure 4.2 with the average measured value in red and the standard deviation bound by the shaded grey region. Values were sporadic from RT to 150 °C and were excluded from

Figure 4.2. This is most likely due to the influence of measurement noise on the first derivative for small values of the PLC. The CTE ranged from $(5.1\pm0.2)\times10^{-6}$ K^{-1} at 200 °C to $(9.0\pm0.4)\times10^{-6}$ K^{-1} at 1600 °C. A comparison with the CTEs of W, Mo and HfN is shown in Figure 4.3 along with estimates of the CTE from the rule-of-mixtures (ROM) and inverse rule-of-mixtures (IROM)

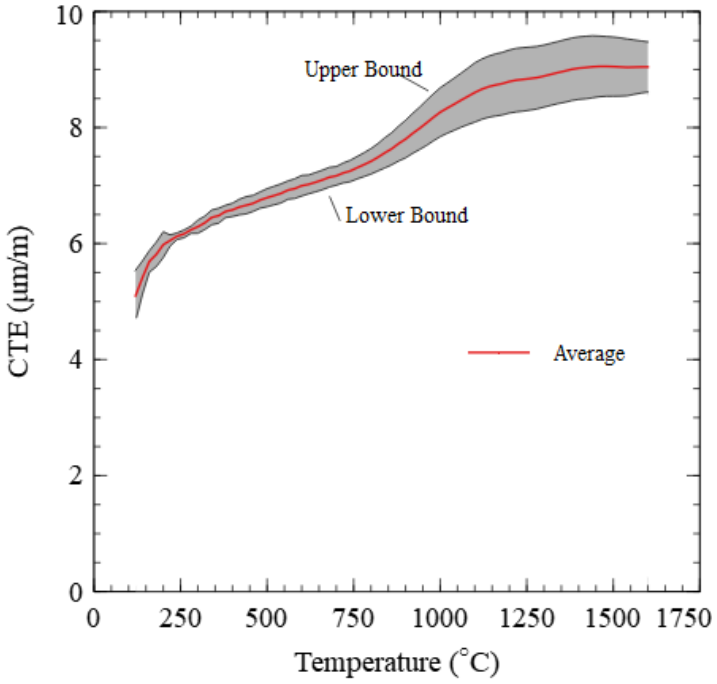

Figure 4.2. CTE of MoW-HfN measured from 25 to 1600 °C. The red line shows the average value with the grey area bounding the standard deviation.

Across the measured temperature range, the CTE of the cermet falls between the CTEs of HfN, Mo, and W. Though data for HfN is limited, both the ROM and IROM provide reasonable quantitative descriptions of the CTE of the cermet in the 200-700 °C range. However, unless there is a significant increase in the CTE of HfN above ~800 °C

it is difficult to see how the ROM or IROM could describe the “hump” in the data above 800 °C.

One possible explanation for the hump-like feature is that above 800 °C, thermal expansion is driven primarily by expansion of the HfN particles. Given the relative difference in CTEs between HfN, Mo, and W, it is plausible that thermal microstrain forms at the particle-matrix interface as the billet cools from sintering temperatures. Considering the sintering temperature of 1800 °C mid-point CTE values of about 8.5×10^{-6} K^{-1} and 4.5×10^{-6} K^{-1} could be used to make a rough estimate of the volume change for HfN and W, the two components with the greatest difference in CTE. Assuming zero strain at 1800 °C, the net percent volume change for HfN at room temperature is about -4.5% and -2.4% for W. Mo is intermediate to HfN and W.

Therefore, as the cermet cools, the HfN particles contract more than the metal matrix placing the particle-binder interface in tension and/or causing microcracks to form. It is plausible to suspect that thermal expansion of the HfN particles at lower temperature is at least partially compensated for by a release of the tensile stress at the interface or of microcrack closing. As the material is again heated, the differences in thermal expansion between metal binder and ceramic particle decrease and the outward force of the particle on the binder is felt more easily, hence the CTE of the cermet is more similar to that of the HfN at elevated temperatures. In short, the simple ROM probably does not capture the effect of diminishing difference in volume mismatch between particle and binder as the temperature of the cermet is increased. This idea will be revisited in the discussion of mechanical properties.

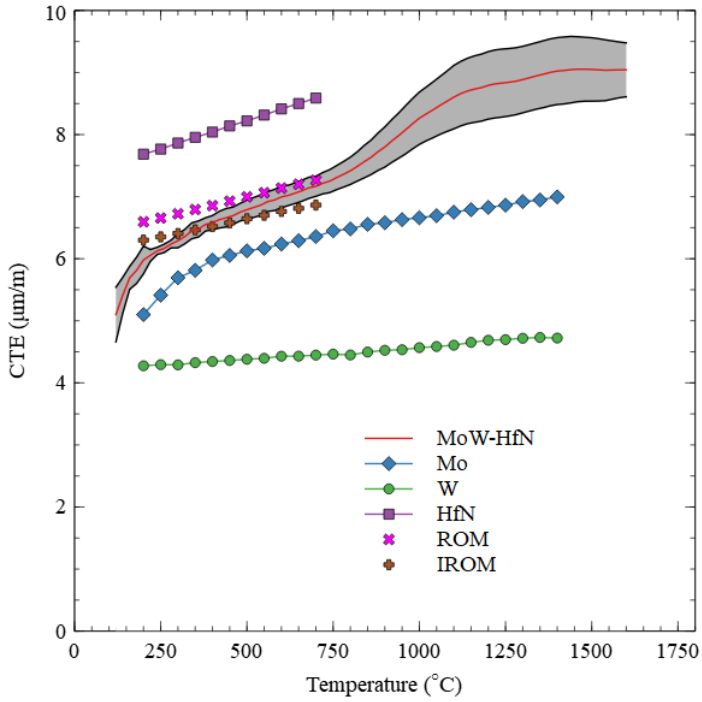

Figure 4.3. Comparison of measured CTE to CTE of constituent parts and ROM/IROM models [36, 53].

4.2. SPECIFIC HEAT CAPACITY

Specific heat measurements using the laser flash technique are shown in Figure 4.4. Specific heats for HfN, Mo, and W obtained from the literature are also shown as is a ROM calculation. Above ambient temperatures and over length scales greater than nanometers, specific heat can be considered an intensive and intrinsic material property. As such, it is expected that the ROM provides an accurate estimate of the specific heat of a composite. Indeed, the data points at 200 and 600 °C agree well with the ROM. The higher temperature data is not reliable for reasons that the specimens reacted with the carbon coating during the laser flash measurements.

As mentioned in the methodology section, it was found that the specimens react with carbon above 600 °C. Even if the reaction layer doesn't penetrate deep into the

specimen altering the specific heat of the bulk, it is assumed in a laser flash measurement that the absorbance and emissivity of the specimen are constant and representative of carbon, the coating material. As the reaction layer forms and consumes the carbon layer, the coating is replaced with a new material with a different (and possibly changing) emissivity and absorbance. Thus, the data at 1000 and 1400 °C are not physically meaningful and should be ignored. While the specific heat data are incomplete, the two lower temperature data help validate the ROM calculations.

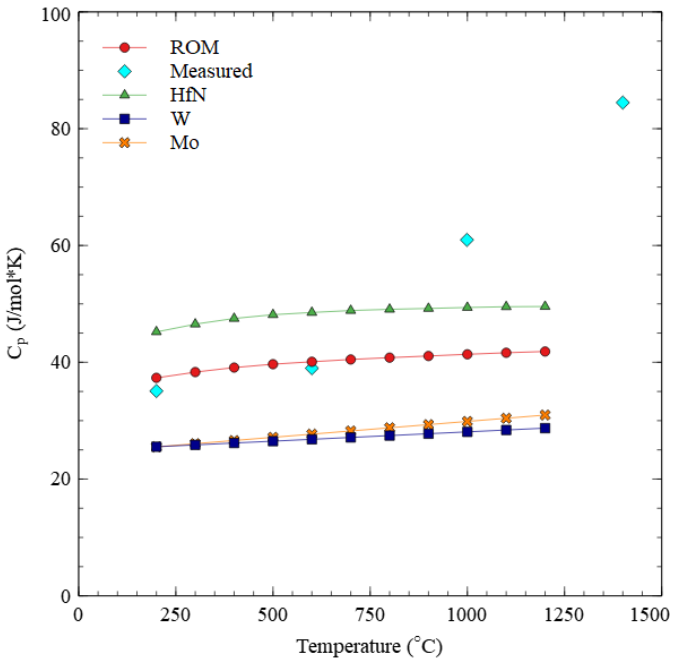

Figure 4.4. Specific heat capacity measured from DSC, compared to ROM and laser flash measurements.

4.3. THERMAL DIFFUSIVITY AND CONDUCTIVITY

The measured values for the thermal diffusivity are shown in Figure 4.5. Measurement were performed both during the ramp up and ramp down to/from the

maximum temperature. An initial value of 0.17 $cm^2 s^{-1}$ was measured at RT and decreased, slightly to 0.16 $cm^2 s^{-1}$ at 1800°C. On the ramp down, a slight hysteresis was observed. The maximum diffusivity measured on ramp down was 0.19 $cm^2 s^{-1}$. This hysteresis could be a result of a change in the microstructure brought about from heating the specimen or from thermal cycling of the specimen.

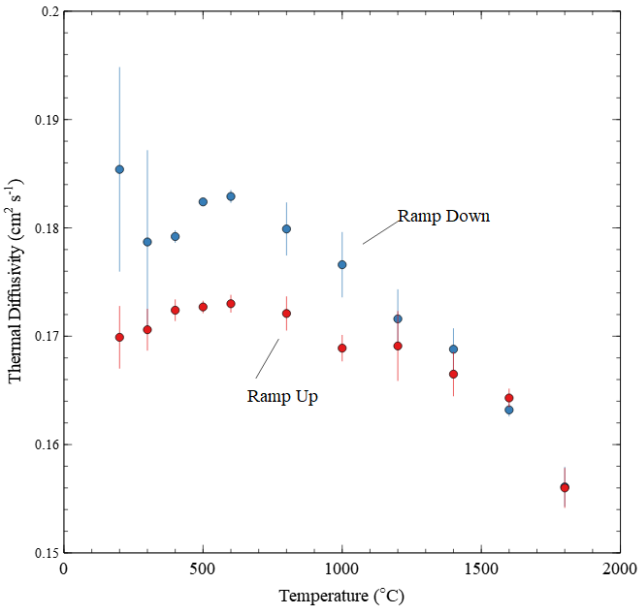

Figure 4.5. The thermal diffusivity measured up to 1800°C. A slight hysteresis can be seen between measurements taken ramping up and cooling down.

Using the measured thermal diffusivity, measured percent linear change, and the heat capacity obtained from the ROM (and experimentally validated up to 600 °C), a semi-empirical calculation can be obtained for the thermal conductivity of the cermet using Equations 4.1 and 4.2:

$$k(T) = C_p(T)\rho(T)\alpha(T) \qquad \text{Equation 4.1}$$

$$\rho(T) = \frac{\rho_0}{1+3\left(PLC/_{100}\right)} \qquad \text{Equation 4.2}$$

where k is the thermal conductivity, C_p is the specific heat capacity, ρ is the density, α is the thermal diffusivity, and PLC is the percent linear change.

Figure 4.6 below shows the resulting calculation compared with the ROM, IROM, and Bruggeman model. It can be seen in Figure 4.6a that the thermal conductivity of the cermet falls between the thermal conductivities of HfN, Mo, and W. Since HfN has a relatively low thermal conductivity compared to Mo and W and a larger effective volume, k_{eff} is significantly lower than those of the metals, 46±6 W m^{-1} K^{-1} at 200 °C and 48± 6 W m^{-1} K^{-1} at 1200 °C.

The ROM (Figure 4.6b) model overestimates k_{eff}, ranging from 63.2 W m^{-1} K^{-1} at 400 °C to 52.7 W m^{-1} K^{-1} at 1200 °C. Similarly, the IROM (Figure 4.6d) underestimates the thermal conductivity, staying relatively constant at 23-25 W m^{-1} K^{-1}. The Bruggeman model (Figure 4.6c) shows the best agreement with the data, ranging from 50 W m^{-1} K^{-1} at 400°C to 43 W m^{-1} K^{-1}at 1200°C. Within the range of temperature for which literature data was available for calculating the Bruggeman result, the model falls within one standard deviation of the data. As with other cermet nuclear fuels with similar ceramic volume fractions, the Bruggeman model proves to be effective at predicting k_{eff}. Knowing this, Equation 2.6 may provide useful for predicting the thermal conductivity of HfN-MoW and UN-MoW cermets with somewhat different metal and ceramic volume fractions. That said, the Bruggeman model is still somewhat crude in that it does not

consider the particle size or shape nor contact resistance between the metal and ceramic phases.

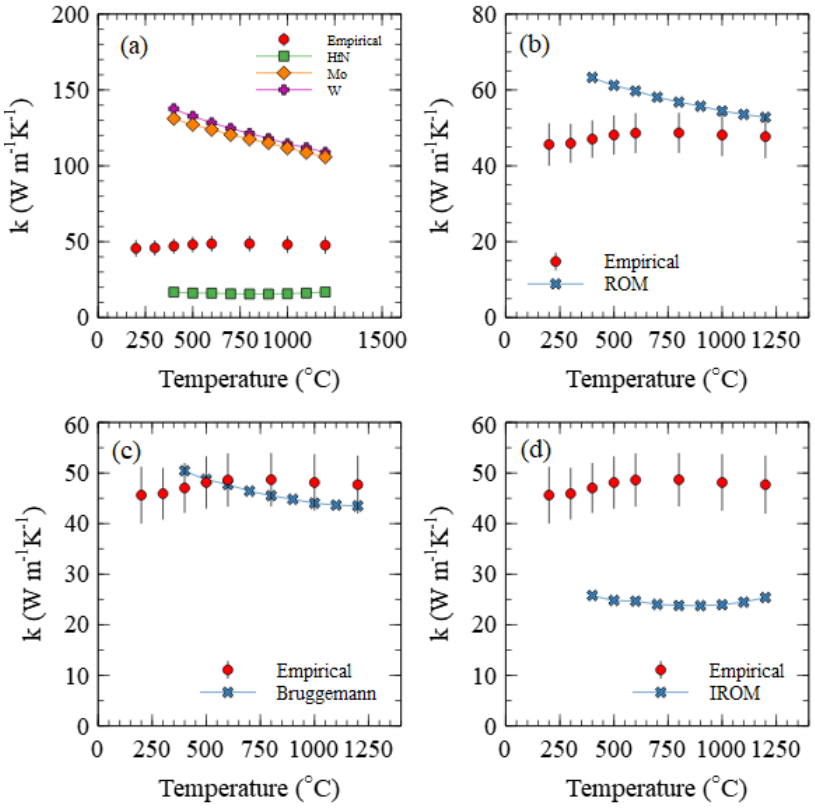

Figure 4.6. Semi-empirical thermal conductivity, k_{eff}, of the cermet compared to a) those of its constituents, b) the Bruggeman model, c) the inverse rule-of-mixture (IROM), and d) rule-of-mixture (ROM) models [45, 53, 54].

4.4. MICROSTRUCTURE ANALYSIS

4.4.1. Optical Microscopy. A representative micrograph, taken in diffuse lighting, is shown in Figure 4.7. The light grey regions are HfN and the blue grey regions are the MoW alloy. Prior microstructural analysis, the density of the specimen was obtained using the Archimedes method. The measured bulk density was 11.77 g cm^{-3}.

Comparing that result to the cermet theoretical density of 13.46 g cm^{-3}, obtained from the theoretical densities of HfN, Mo, and W, gives a porosity of ~12%. Figure 4.7 and images taken in direct lighting conditions confirm there is considerable porosity present in the specimen (black features). The porosity tends to be found in and near agglomerates of the larger HfN particles and/or along the ceramic metal interfaces. A wide distribution of HfN particles can be seen from this image, mainly comprising larger HfN particles on the scale of tens of microns effective radius with smaller HfN particles dispersed through the MoW matrix.

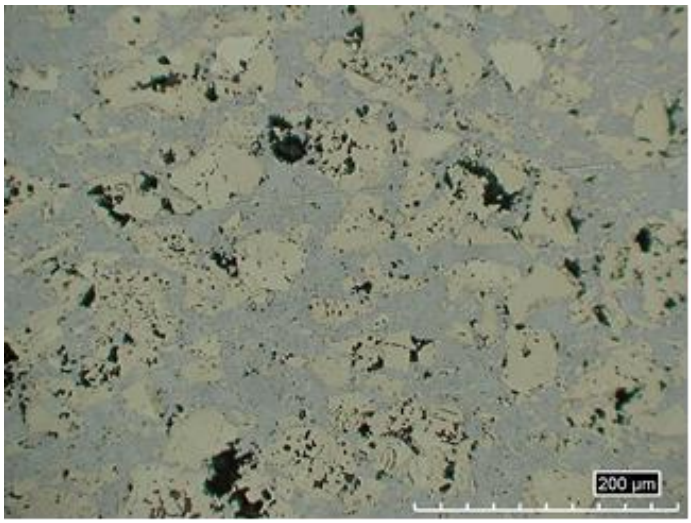

Figure 4.7. Optical image of cross section taken at low magnification. Black is assumed to be porosity, light grey is the HfN, and blue grey the MoW alloy.

4.4.2. SEM Microscopy and EDS. Figure 4.8 below shows the SEM image and EDS composite maps obtained. EDS maps for Hf, Mo, and W are layered over the micrograph by color, blue for Hf, green for Mo, and pink for W.

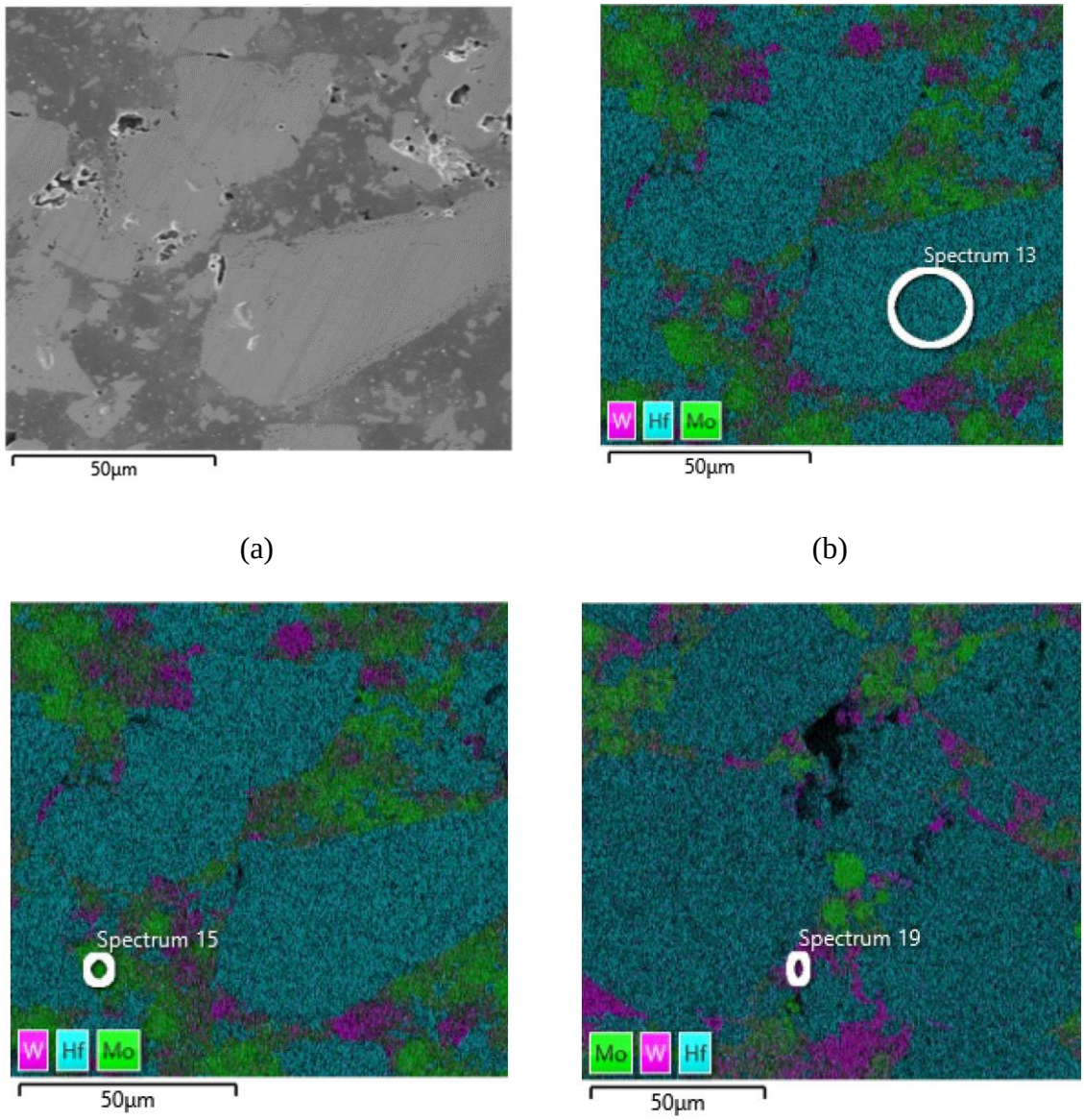

Figure 4.8. SEM micrographs of specimen. a) SEM image 4 and b), c), d) EDS layered image. The corresponding EDS spectra can be seen in Appendix.

As expected, the light grey particles in the optical microscope images were the Hf rich cermet particles and the surrounding blue grey material the MoW matrix. An

interesting feature revealed by the EDS map is the appearance of distinct regions of Mo and W, seen in both EDS images. This is believed to be due to the separate Mo and W powders being used in the billet preparation.

4.4.3. Particle Analysis. Two separate particle analyses were done; one for the larger HfN particles, and another for the smaller HfN "debris" seen dispersed uniformly in the metal matrix. Figures 4.9 and 4.10 show the resulting particles selected for particle analysis from the SEM images.

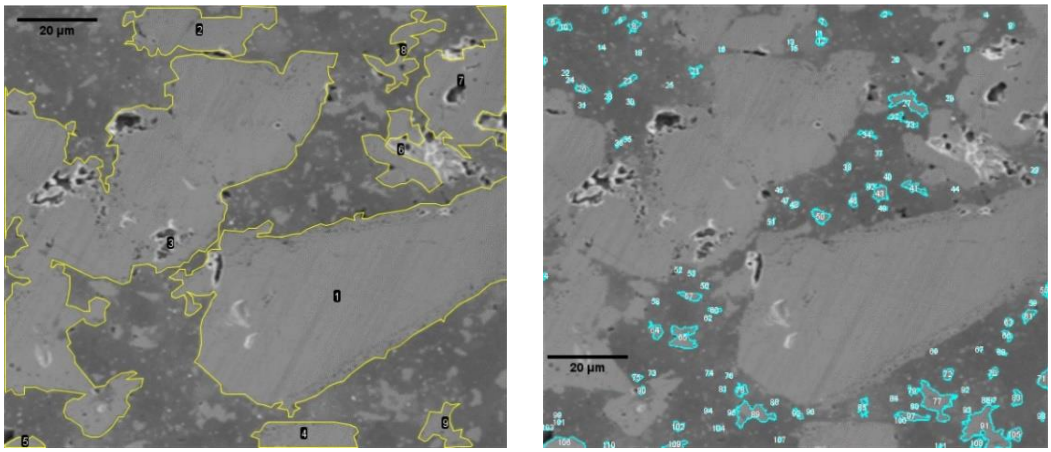

(a) (b)

Figure 4.9. Particle selections for a) large HfN and b) small HfN particles

The larger particles were manually selected, while the smaller particles were selected using an automatic thresholding algorithm. The MinError(1) method was used for smaller particles, with the areas constrained from 0.5-68.3 μm^2 and 1-100 μm^2 for Figure 4.9b and Figure 4.10b respectively, and circularity ranging from 0-1.

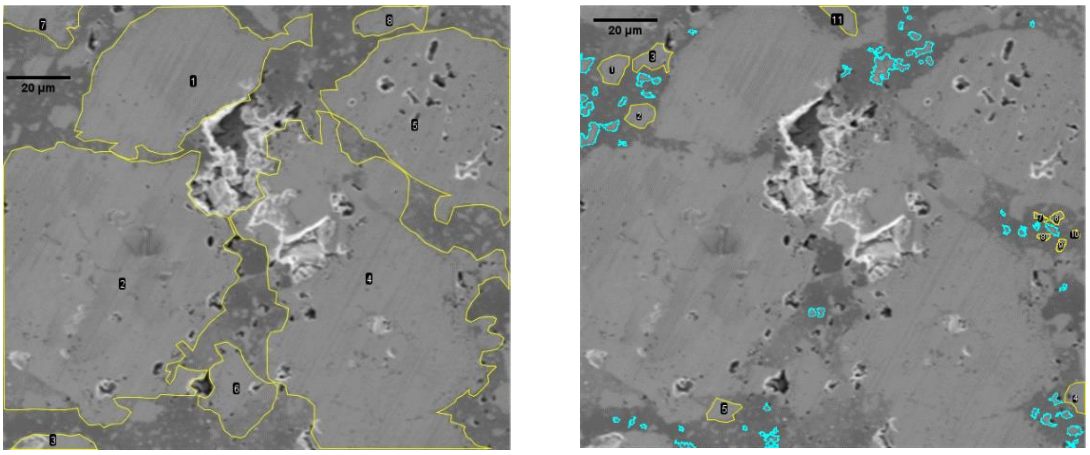

(a) (b)

Figure 4.10. Particle selections in for a) large HfN particles and b) small HfN particles

For the larger particles, an average area of 1300 µm^2 was calculated, assuming spherical particles. This gave an effective diameter of about 30 µm. Table 4.1 below summarizes the median, upper, and lower quartiles for the HfN particles. Since the sample population is small (17 total particles), the results are widely distributed and only give a rough estimation of the particle size. Outliers can easily skew the mean, so the median was also calculated, with larger particles having a median area of 320 µm^2 and smaller particles having a median area of 4 µm^2. Quartiles are also provided to give an effective range of the particle area. Analysis of the optical image can give a bigger sample size and therefore more quantitative results.

Due to the small particle count from the SEM images, a more accurate distribution could be obtained via processing the optical image. This larger scale of the microstructure allows for more particles to be included. The qualitative result is the same, however. Overall, both methods show that the larger particles correspond to the

nominally sub-45 μm starting HfN powder used during process. The smaller particles had an average area and diameter of 4 μm^2 and 2 μm. The median area was 2 μm^2 and median diameter was 1.5 μm.

Table 4.1. Median, upper, and lower quartile obtained for area of HfN particles

	Large Particles		Small Particles	
	Area (μm^2)	Diameter (μm)	Area (μm)	Diameter (μm)
Mean	1300	30	4	2.0
Median	320	20	2	1.5
Lower Quartile	150	14	1	1.0
Upper Quartile	2300	54	4	2.3

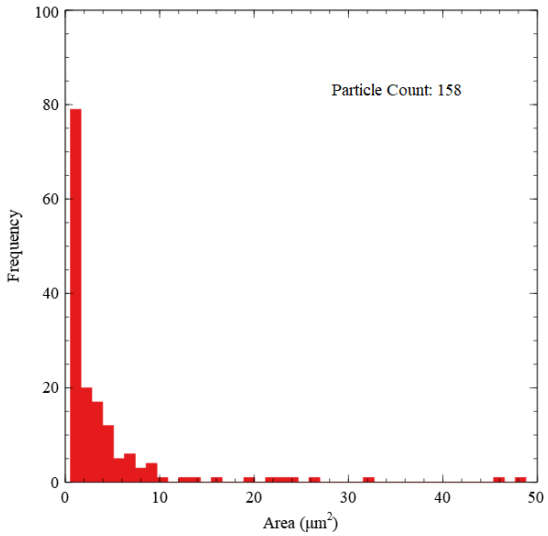

Figure 4.11. Distribution of smaller HfN particles

Figure 4.11 above shows the particle size distribution for all particles analyzed. The distribution is highly skewed due to the presence of the small particle "debris." It is possible that the larger particles are more-or-less centrally distributed but given the degree of agglomeration, it may be difficult to obtain a meaningful particle size distribution even if a larger sample of large particles is analyzed.

4.5. MECHANICAL PROPERTIES

Figure 4.12 shows the elastic modulus as measured in bending and the maximum stress measured from room temperature up to 1600 °C. At room temperature, the modulus is 230±10 GPa. At 800 °C, the modulus drops to ~100 GPa and stays relatively constant up to 1400 °C, where it again decreases to 68±1 GPa at 1600 °C. This trend of the modulus decreasing with temperature is expected since as temperature increases the material becomes easier to deform. That said, this measured value of *E*, however, is much lower compared to the moduli of Mo, W and HfN, which are 350, 400 and 380 GPa, respectively, at room temperature. Sources of the error could include the formation of microcracks, compliance within the test fixture, and porosity. Porosity is known to reduce the Young's modulus of materials [55]. Given the billet was shown to have ~12% porosity present, porosity is certainly a plausible contributing factor. Microcracking may be a significant source of error in a flexure measurement as one side of the specimen surface is under tension. With cracks present, the effective cross-sectional area of the specimen perpendicular to a tensile load is reduced. Complementary measurements of the

Young's modulus should be performed using different techniques to determine the validity of the measurement.

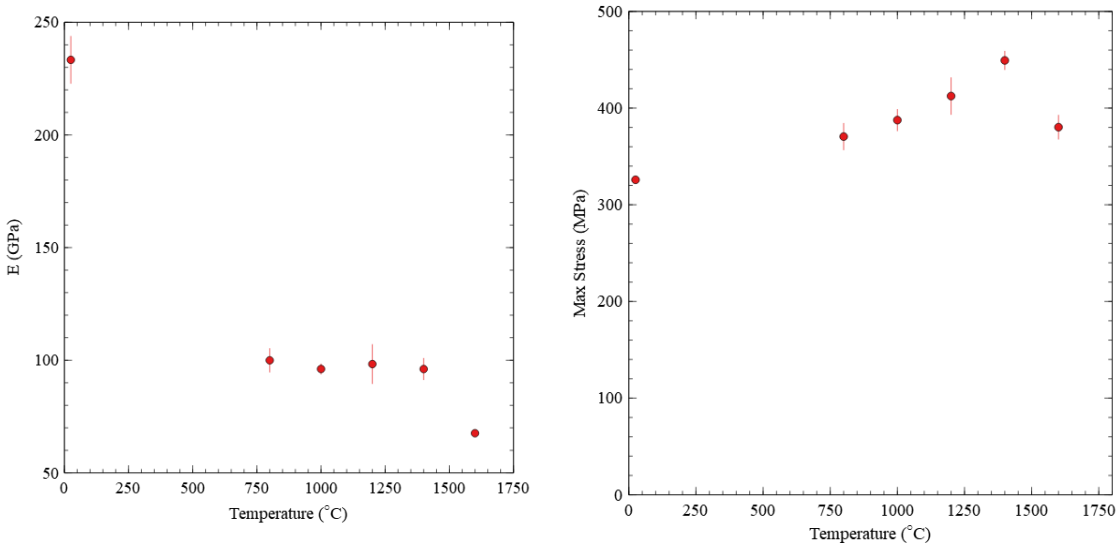

Figure 4.12. The a) average elastic modulus and b) average failure stress up to 1600°C

As temperature increases, the maximum stress was observed to increase from 325±4 MPa to 450±10 MPa until 1400 °C, where it then fell to 380±10 MPa. One possible explanation for the increase in maximum stress is that after processing and machining the bars, residual stress remains. As seen in earlier, there is a significant CTE mismatch between the binder and HfN. It is reasonable to assume low initial microstrain at the sintering temperature (1800 °C). Upon cooling, the HfN (having a larger CTE) will contract more than the binder, placing the particle binder interface under tension, and concentrating stresses in the microstructure, especially near the metal-ceramic interface.

Though no microcracking was observed in the micrographs, concentrated stresses could lower the critical load on the specimen by enhancing the stress intensity around microstructural features. With this residual stress left over in the cermet, the applied stress needed for cracks to propagate is effectively lower. By increasing the temperature towards the sintering temperature (1800 °C) it is possible that microstrain is partially removed as the HfN and binder thermally expand to their initial unstrained state. Thus, a higher externally applied load is needed to achieve stress intensity factors to allow cracks to propagate.

An alternative explanation of the increase in maximum stress is that there were morphological changes to the specimen surface during testing, due to for example reaction of the surface with the furnace atmosphere. This hypothesis supposes that the critical flaw resides at the surface and changes to the surface or near-surface microstructure alter the shape of the critical flaw. Indeed, there were visible differences in the color and surface appearance of the broken bars. It is unclear if this occurred during testing or was a result of exposing the specimens to air upon cooling from ~500 °C to RT. Unfortunately, fractography measurements (see Appendix) did not reveal a clearly identified critical flaw at either the surface or from within the bars. Additional measurements should be conducted to better identify the failure origin.

In the MoW strength vs. temperature curves shown in Figure 2.8 an inflection point exists around 1400 °C. Above that point, there is a pronounced drop in yield strength accompanied by an increase in the percent elongation. This indicates that the metal binder is becoming softer and more ductile, allowing the cermet to deform more easily. 1400 °C roughly corresponds to the point at which the maximum strength in

bending begins to decrease. This suggest that the loss in strength above 1400 °C is due to the onset of plastic deformation in the binder. It is interesting to note that pure Mo loses strength about 300 °C before W or any of the MoW alloys shown in Figure 2.8. This suggests that in the present material, the Mo begins to plastically deform before the W. It also suggests that a well alloyed MoW binder would show improved high temperature strength. That said, the thermal conductivity of the MoW alloy is lower than that of Mo and W separately [54], so a well alloyed metal binder, while having improved strength may have a lower thermal conductivity. Future work will be needed to compare both the mechanical and thermal properties of HfN-MoW cermets made with separate Mo and W starting powders and with well alloyed MoW starting powder.

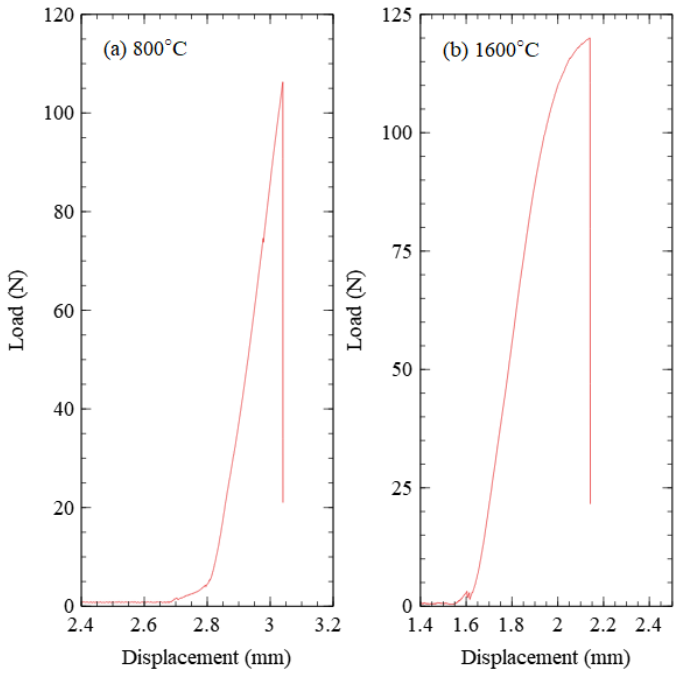

Figure 4.13. The load vs displacement curves at a) 800°C and b) 1600°C.

In the load vs. displacement graphs, a sharp linear point at failure indicates that the material was loaded at a sufficiently fast rate to fail in the linear elastic regime. At the higher temperatures, the onset of plasticity, and time-dependent phenomena such as creep, and slow crack growth can interfere with measurements, resulting in a different physical interpretation of the results. For most temperatures, this was corrected for by increasing the crosshead speed. At 1600 °C, this nonlinearity was observed even at crosshead speeds of 2.5 mm/min, shown in Figure 4.13. The rounding of the curve is consistent with the above explanation invoking the onset of plasticity in the metal matrix.

A noticeable bend was also observed in the flexure bars after testing that was not present during relatively lower testing temperatures, further showing that some plastic deformation occurred before fracture. This can be seen in Figure 4.14, where bars from room temperature, 1000°C, 1400°C, and 1600°C are lined up from top to bottom.

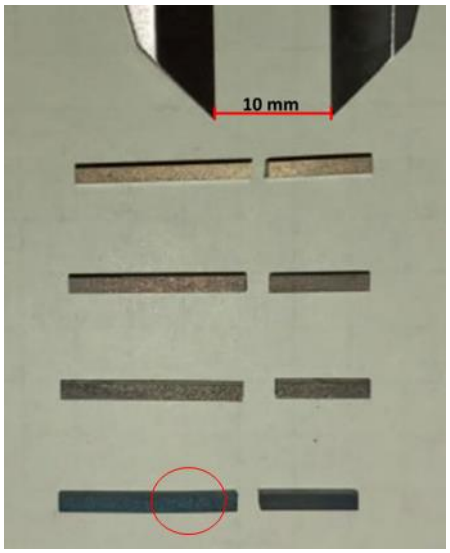

Figure 4.14. Flexure bars after testing, arranged from top to bottom as 25°C, 1000°C, 1400°C and 1600°C. A noticeable bend can be seen in the 1600°C bar in the circled area.

At lower temperatures no noticeable deflection is seen. At 1600 °C a slight bend can be seen near the fracture half of the bar. This provides additional evidence that the loss of strength above 1400 °C is due, in part, to the onset of plastic deformation in the metal binder.

5. CONCLUSION AND FUTURE WORK

To effectively model reactor and fuel performance in a Nuclear Thermal Propulsion system, a thorough understanding of the properties and behavior of the fuel and reactor materials under extreme operating conditions must be developed. NTP reactor design uses a coupled Multiphysics modeling approach that considers, among other things, the thermal and mechanical properties of the materials. The predictive power of such models, however, is only as good as the accuracy and validity of the underlying materials property data or constitutive models. A lack of empirically obtained thermal and mechanical property data for UN-MoW cermets, and its separate components, calls for a need to better characterize those materials.

This study represents one of the first efforts to experimentally characterize the thermal and mechanical properties of the cermet MoW-HfN, a surrogate material for MoW-UN fuel. It establishes a basic set of material property data that can be used in future efforts to model NTP systems. It will also help validate computational materials models being developed to predict the properties of such materials. This work also helps establish research methods that can be built upon in future studies of cermet fuels. Specific materials properties characterized in this work include: the coefficient of thermal expansion, thermal diffusivity, modulus of bending, and specific heat capacity. These properties were correlated with the composition and microstructure.

The microstructure was shown to consist of a distribution of larger HfN particles with sizes averaging about 32 μm, with smaller HfN particles, about 1-2 μm in diameter, dispersed throughout the metal matrix. A bulk density of 11.76 g/cm^3 was measured,

88.6% of the theoretical density. EDS revealed areas of mostly pure Mo and W heterogeneously dispersed throughout matrix, most likely the result of processing the cermet using separate Mo and W powders.

Push rod dilatometry measurements resulted in thermal expansion coefficients (CTE) between 5-9×10^{-6} K^{-1} in the temperature range 200-1600 °C. HfN has a higher CTE compared to Mo and W. While both the rule-of-mixtures (ROM) and inverse rule-of-mixtures (IROM) proved to be reasonably accurate at predicting the CTE of the cermet within the range of 200-700 °C, it is unclear whether such models are valid at higher temperatures. Trends in the data possibly suggest that the HfN has a greater influence on the CTE above 800 °C.

Laser flash measurements show that the thermal diffusivity falls in a narrow range from 0.17 cm^2 s^{-1} at 200 °C to 0.16 cm^2 s^{-1} at 1800 °C, and shows only slight hysteresis ramping up and down in temperature. Initial tests used a graphite coating resulted in a surface reaction layer forming. While this did not present a problem for determining the specific heat capacity at temperatures below 600 °C, it confounded results at higher temperatures. Etching the specimens in 3% HF acid was found to be a useful alternative to enhancing the absorption characteristics of the specimens without introducing additional carbon. Such a technique is only applicable to thermal diffusivity measurements. The lower temperature laser flash measurements using coated specimens, however, showed that a simple ROM is adequate for predicting specific heat. The ROM specific heat, measured CTE, and measured thermal diffusivity were used to calculate a semi-empirical thermal conductivity. The semi-empirical thermal conductivity was found to be in good agreement with predictions made using the Bruggeman model.

Four-point flexure tests showed that the modulus of elasticity at room temperature is around 230 GPa and drops to below 100 GPa at elevated temperatures. These values are significantly lower than the moduli of the constituent materials. It is suspected that microcracking from CTE mismatch, residual stress in the bar, porosity, or compliance in the test fixtures are responsible for unexpectedly low values. Complimentary testing using an alternate technique is needed to confirm those results. An increase in maximum stress was observed as temperature increased up to 1400 °C. This is attributed to either the presence of microstrain caused by the CTE mismatch, or to changes to the surface condition of the test specimens in the furnace. Plastic deformation was observed at 1600 °C. This is consistent with the loss of strength in both W and Mo at temperatures above 1400 °C. Future work should be performed to measure residual stress as a function of temperature using X-ray or neutron diffraction. Chevron notch test are also recommended for estimating the critical flaw size range and better understand the failure mechanism.

As this work was conducted using a surrogate material, the thermal properties of the UN cermet are expected to be slightly different. Thermal conductivity is not expected to change much since UN has only a slightly higher conductivity (~25 W m^{-1} K^{-1}) than HfN (~20 W m^{-1} K^{-1}). In terms of mechanical properties, the Young's modulus is expected to be expected to be lower in UN-MoW than in HfN-MoW, UN having a smaller Young's modulus than HfN. As UN has a higher CTE compared to HfN, a greater CTE mismatch is expected. Some of the thermomechanical effects discussed in this work may be accentuated in the case of UN-MoW.

APPENDIX

1. NEUTRON ABSORPTION CROSS SECTIONS

Table A1. Abundances and absorption cross sections of Mo and W isotopes [31]

Isomer	Abundance	Thermal Absorption Cross-section (b)
Mo-92	14.649%	0.08
Mo-94	9.187%	0.34
Mo-95	15.873%	13.4
Mo-96	16.673%	0.5
Mo-97	9.582%	2.2
Mo-98	24.292%	0.13
Mo-100	9.744%	0.199
W-180	0.12%	30
W-182	26.5%	20.7
W-183	14.31%	10.1
W-184	30.64%	1.7
W-186	28.43%	37.9

2. FRACTOGRAPHY

Using a Hirox Optical Microscope, several images of the fracture surfaces were obtained for broken flexure specimen bars tested at room temperature, 1000 ºC, 1200 ºC and 1600 ºC. Images were taken at low magnifications, starting at 100x. Since the depth of field is smaller on optical microscopes, parts of the bar were out of focus, making analysis difficult. This was resolved by using semi-auto focus mode to create a fully focused image. Upper and lower limits were set for the focal planes, which were then split into 50 different images and composed to make a fully focused image., shown in Figure A1 below. A 3D reconstruction of the image surface is also made in the process, allowing for a more detailed image of the surface to be obtained.

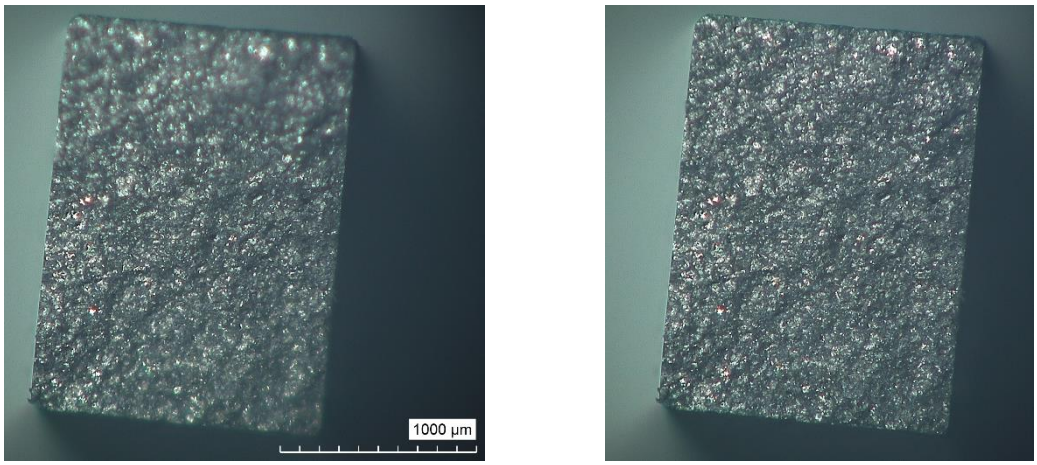

Figure A1. Optical image of fracture bar tested at room temperature, before(left) and after(right) using the semi-auto focus mode. Though in focus, little to no features are discernable from the microstructure, specifically the hackle lines used to locate the fracture origin.

An external light source was shined at a low angle on the surface to help emphasis 3D features that couldn't be easily seen. This is shown below in Figure A2.

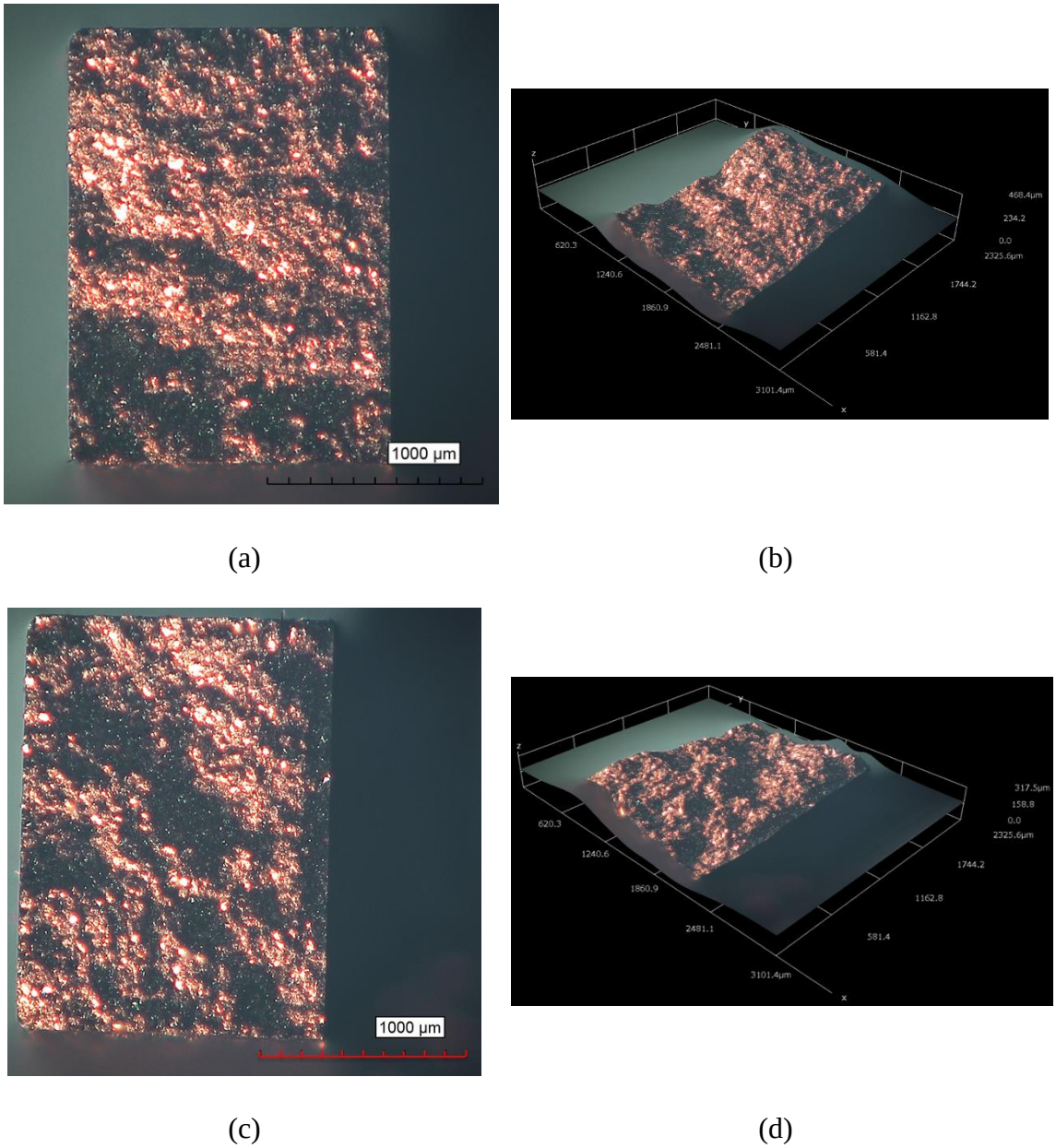

(a) (b)

(c) (d)

Figure A2. Diffused lighting optical microscopy done at 100x magnification with an external light source for contrast on a) Bar 3 and its b)3D composite image, along with c)Bar 4 and its 3D composite image. No visible hackle lines are present.

To get an approximate size of the crack flaw and be able to correlate to possible microstructure features, chevron notch toughness should be performed. By finding fracture toughness, K_{IC}, from a crack of known size, a range of estimated flaw sizes can be back calculated for the flexure bars for different Y values (different flaw geometries).

3. THERMAL DIFFUSIVITY

The thermal diffusivity was originally performed applying a graphite coating to the specimen. It can be seen below in Figure A3 that significant hysteresis was observed upon performing the measurements on ramp up and ramp down. A later experiment was conducted where a sacrificial sample was placed on graphoil in a furnace. Upon removing the sample, the sample had bonded to the graphoil indicating that the specimen forms a reaction layer with carbon.

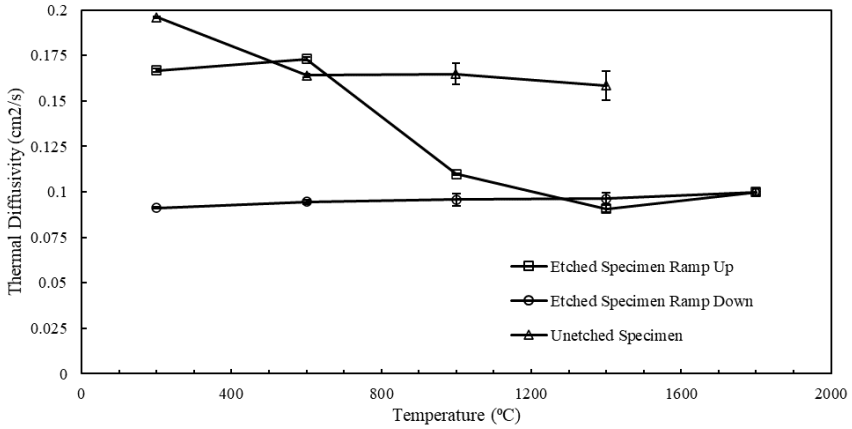

Figure A3. Thermal diffusivity samples with graphite coating.

4. EDS SPECTRA

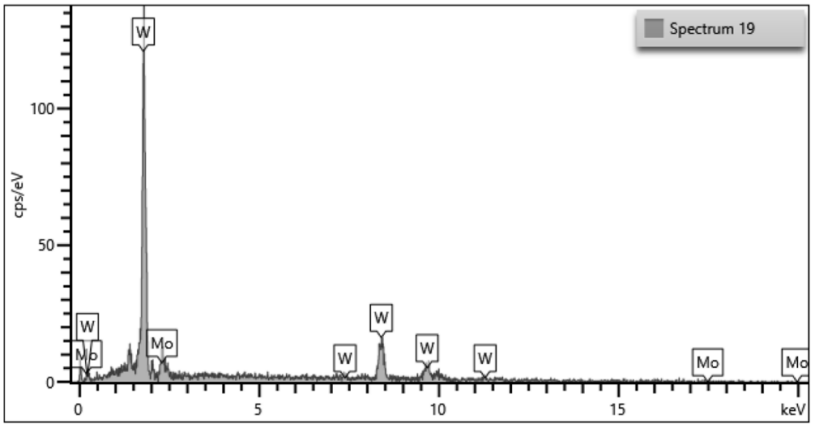

Spectrum 19							
Element	Line Type	k Ratio	Wt%	Atomic %	Standard Label	Factory Standard	Standard Calibration Date
Mo	L series	0.13838	10.00	17.56	Mo	Yes	
W	L series	2.53655	90.00	82.44	W	Yes	
Total:			100.00	100.00			

Figure A5. EDS Spectra and relative quantities of W rich area

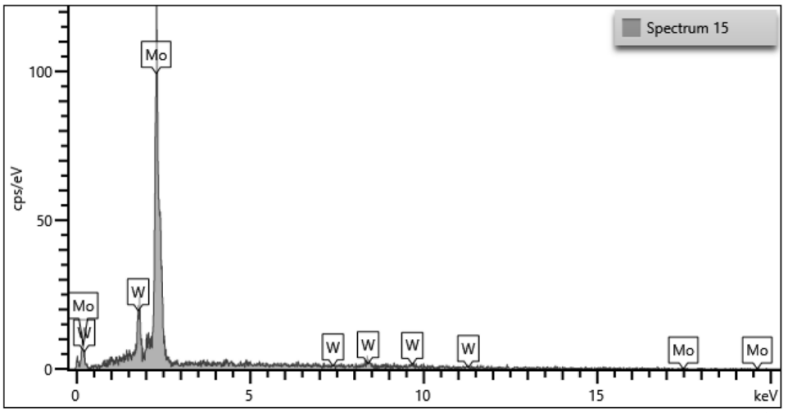

Spectrum 15							
Element	Line Type	k Ratio	Wt%	Atomic %	Standard Label	Factory Standard	Standard Calibration Date
Mo	L series	2.12770	85.64	91.96	Mo	Yes	
W	L series	0.36403	14.36	8.04	W	Yes	
Total:			100.00	100.00			

Figure A6 EDS Spectra and relative quantities of Mo rich area

5. CAD SCHEMATICS

CAD designs for each of the test specimens in Figure A7-A10. Units are in millimeters.

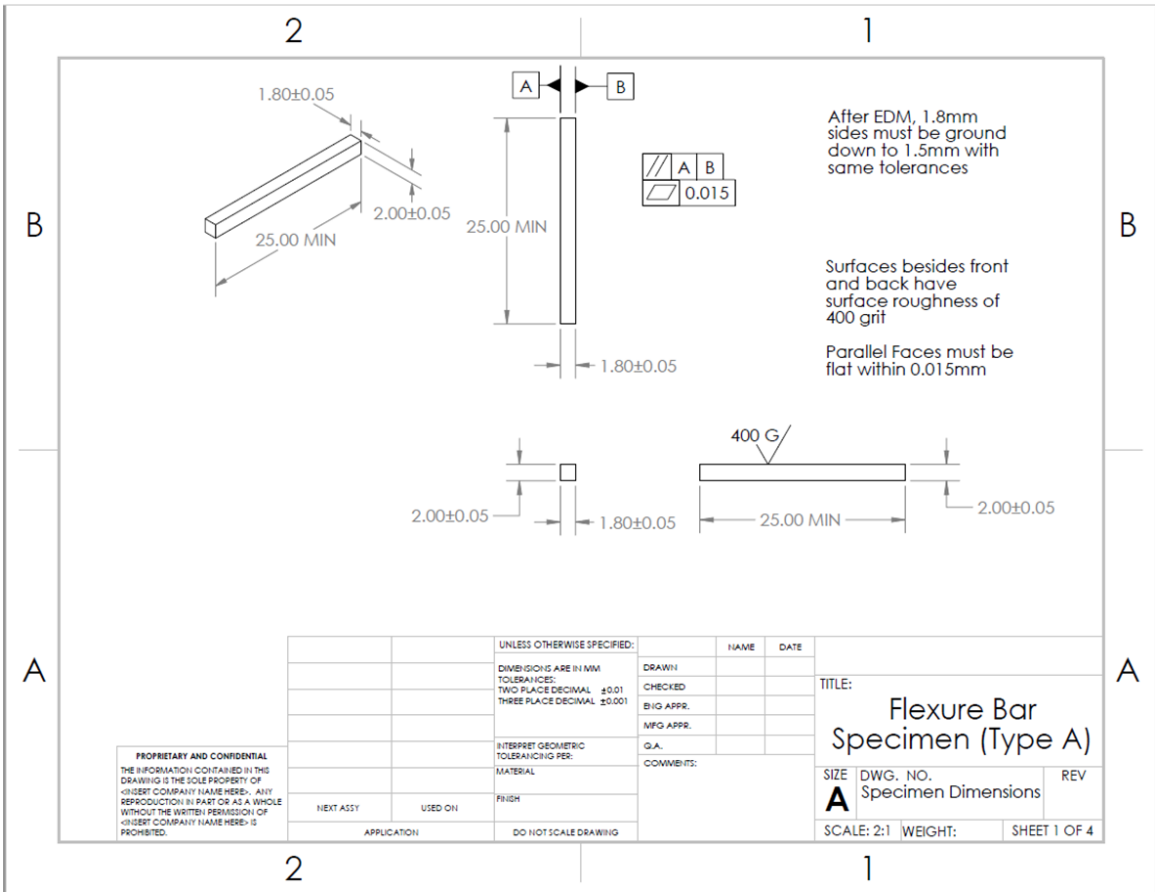

Figure A7. Dimensions and surface finish of Type A Flexure Bars.

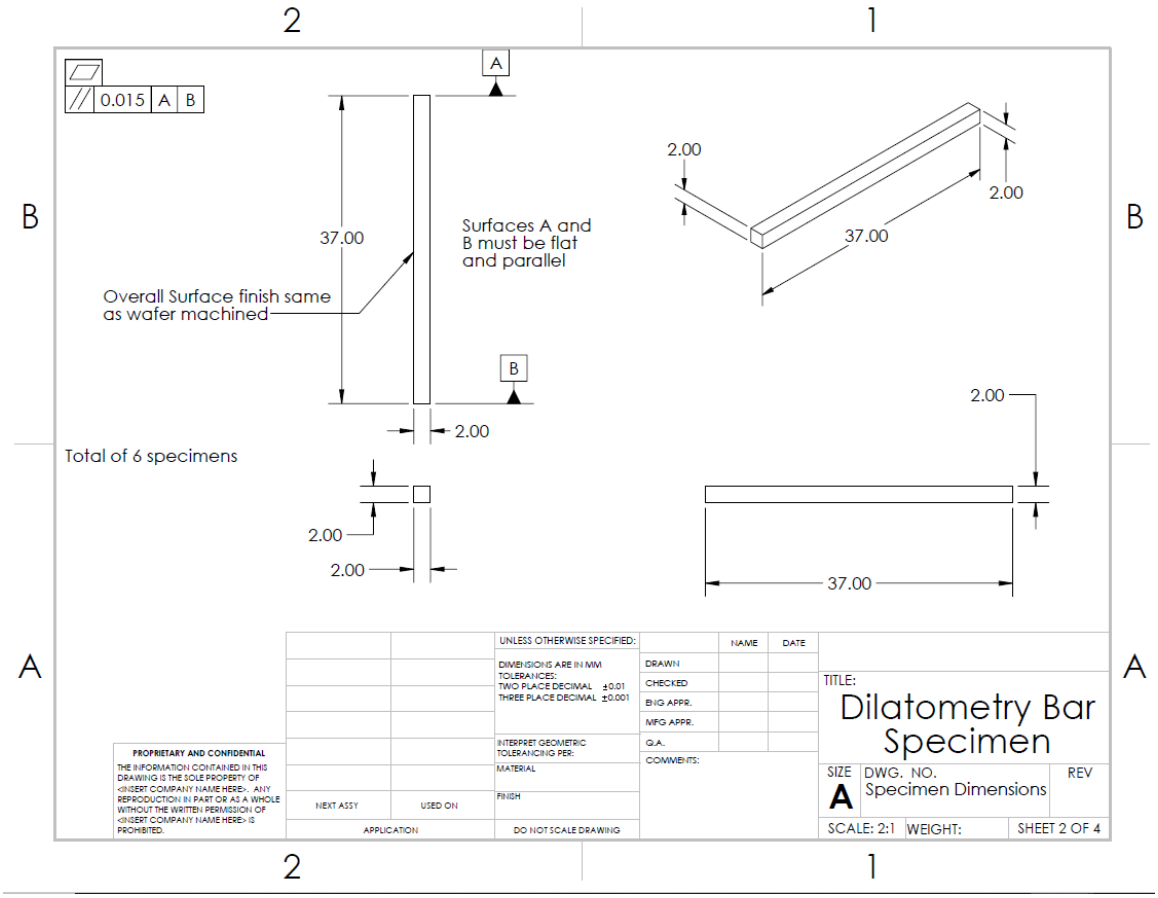

Figure A8. Dimensions and surface finish of dilatometry bars.

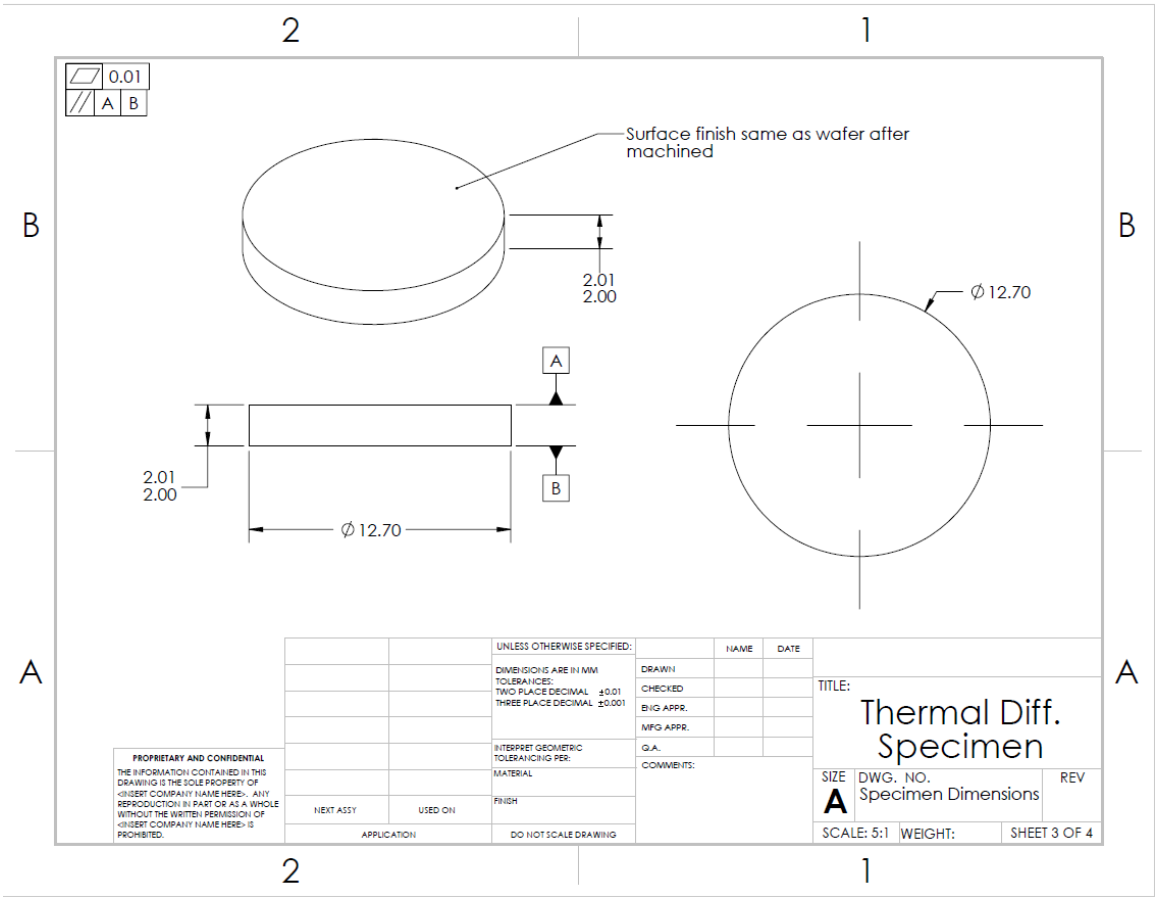

Figure A9. Dimensions and surface finish of laser flash specimens.

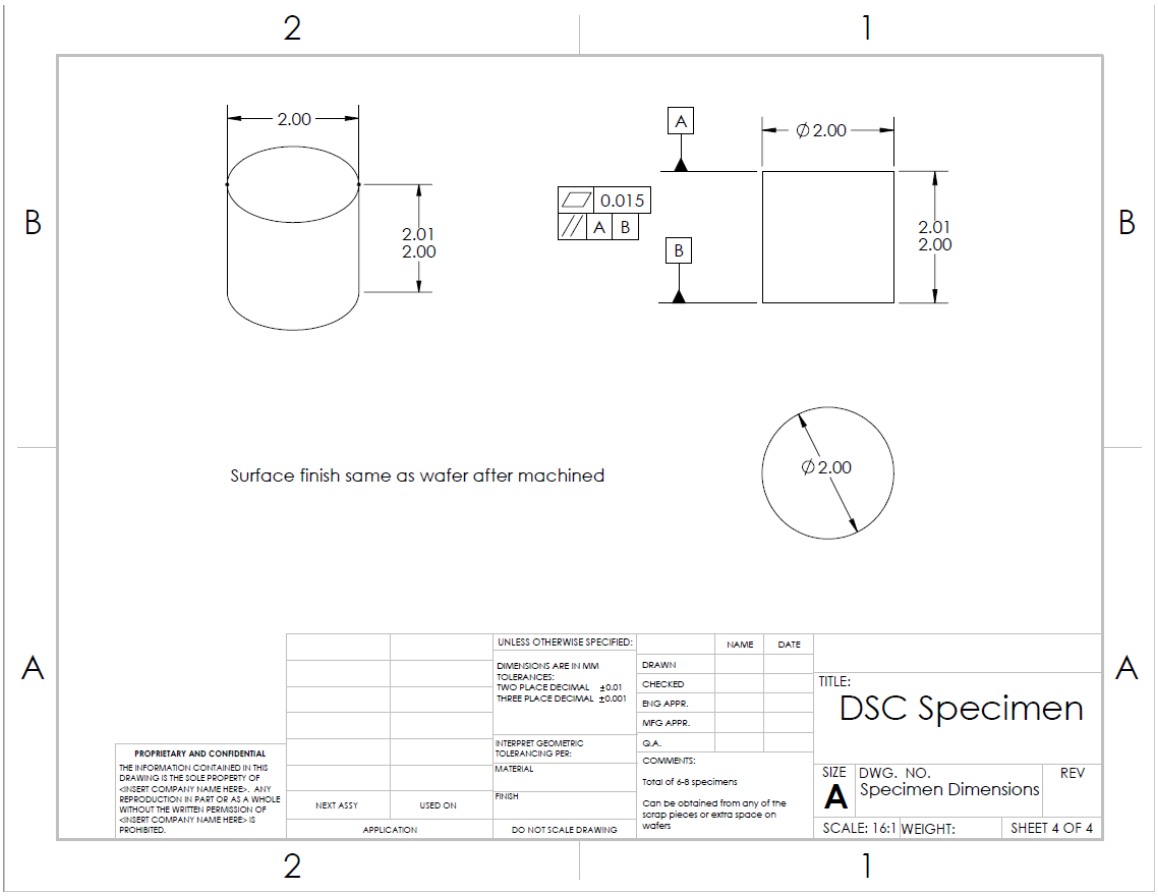

Figure A10. Dimensions and surface finish of DSC specimens.

BIBLIOGRAPHY

[1] Ebersohn, Frans & Raja, Laxminarayan & Shebalin, John. (2013). Resistive Magnetohydrodynamic Study of Magnetic Field Effects on Plasma Plumes. 44th AIAA Plasmadynamics and Lasers Conference. 10.2514/6.2013-2759.

[2] FINSETH, J.L., "Rover nuclear rocket engine program: Overview of rover engine tests", NASA-CR-184270, NASA (1991)

[3] Roland Antonius Gabrielli, Georg Herdrich, Review of Nuclear Thermal Propulsion Systems, Progress in Aerospace Sciences, Volume 79, 2015, Pages 92-113, ISSN 0376-0421, https://doi.org/10.1016/j.paerosci.2015.09.001

[4] Mike Tschiltz. "Addressing the Challenges with Establishing the Infrastructure for the front-end of the Fuel Cycle for Advanced Reactors." NRC. January 2018 https://www.nrc.gov/docs/ML1810/ML18103A250.pdf. NEI

[5] JOHNATHAN A. WEBB; INDRAJIT CHARIT, "Analytical determination of thermal conductivity of W-UO_2 and W-UN CERMET nuclear fuels." *Journal of Nuclear Materials,* **472**, 87, (2012)

[6] Dadić, Zvonimir. (2013). Tribological principles and measures to reduce cutting tools wear.

[7] M. Balog, J. Kováč, A. Šatka, D. Haško, J. Zhang, M.A. Crimp, O. Vávra, I. Vávra, SiC-based cermet with electrically conductive grain boundaries, Materials Characterization,Volume 61, Issue 4, 2010, Pages 420-426, ISSN 1044-5803, https://www.sciencedirect.com/science/article/pii/S104458031000029X

[8] Xu, Ji Fang, et al. "Synthesis and Electrical Properties of Mo-ZrO2 Cermet." Advanced Materials Research, vol. 311–313, Trans Tech Publications, Ltd., Aug. 2011, pp. 2121–2126. Crossref, doi:10.4028/www.scientific.net/amr.311-313.2121.

[9] Antonov M., Pirso J. (2014) Thermal Shock Resistance of Chromium Carbide-Based Cermets. In: Hetnarski R.B. (eds) Encyclopedia of Thermal Stresses. Springer, Dordrecht. https://doi.org/10.1007/978-94-007-2739-7_90

[10] B.G. Compton, F.W. Zok,Impact resistance of TiC-based cermets,International Journal of Impact Engineering, Volume 62, 2013, Pages 75-87,ISSN 0734-743X, https://doi.org/10.1016/j.ijimpeng.2013.06.008.(https://www.sciencedirect.com/science/article/pii/S0734743X1300122X)

[11] Ellis, John L, et al. “Cermets.” *Properties and Selection: Nonferrous Alloys and Special-Purpose Materials*, vol. 2, ASM International. https://doi.org/10.31399/asm.hb.v02.a0001105

[12] Courtney, Thomas H. Mechanical Behavior of Materials. 2nd ed., McGraw-Hill, 2000.

[13] John L. Ellis, Claus G. Goetzel, Cermets, Properties and Selection: Nonferrous Alloys and Special-Purpose Materials, Vol 2, ASM Handbook, By ASM Handbook Committee, ASM International, 1990, p 978–1007, https://doi-org.libproxy.mst.edu/10.31399/asm.hb.v02.a0001105

[14] T. William Clyne, 4.1 An Introductory Overview of Metal Matrix Composites Systems, Types and Developments, Peter W.R. Beaumont, Carl H. Zweben, Comprehensive Composite Materials II, Elsevier, 2018, Pages 1-21, ISBN 9780081005347, https://doi.org/10.1016/B978-0-12-803581-8.09961-6.(https://www.sciencedirect.com/science/article/pii/B9780128035818099616)

[15] Cureton, William F., et al. "Microstructural Evolution of Mo-UO2 Cermets Under High Temperature Hydrogen Environments." Journal of Nuclear Materials, vol. 538, no. C, 2020, pp. 152297.

[16] Webb, Jonathan A., and Indrajit Charit. "Fabrication of Cermets Via Spark-Plasma Sintering for Nuclear Applications." *Jom (1989)*, vol. 66, no. 6, 2014, pp. 943-952.

[17] Johnson A, Jonathan, et al. "Cermet Surrogate Nuclear Fuels from Coated Powders." Journal of Nuclear Materials, vol. 557, 2021, pp. 153246.

[18] Yang, Y., Zhang, C., Wang, D. *et al.* Additive manufacturing of WC-Co hardmetals: a review. *Int J Adv Manuf Technol* **108,** 1653–1673 (2020). https://doi-org.libproxy.mst.edu/10.1007/s00170-020-05389-5

[19] Lengauer, Walter, and Fabio Scagnetto. "Ti(C,N)-Based Cermets: Critical Review of Achievements and Recent Developments." *Solid State Phenomena* 274 (2018): 53-100. *ProQuest.* Web. 23 Nov. 2021.

[20] Simwonis, D., et al. "Properties of Ni/YSZ Porous Cermets for SOFC Anode Substrates Prepared by Tape Casting and Coat-Mix ® Process." *Journal of Materials Processing Technology*, vol. 92, 1999, pp. 107-111.

[21] Mishra, Sudhir, et al. "U-PuO.Sub.2, U-PuC, U-PuN Cermet Fuel for Fast Reactor." *Journal of Nuclear Materials*, vol. 499, 2018, pp. 272.

[22] Talebi, Tahereh, et al. "Investigation on Microstructures of NiO–YSZ Composite and Ni–YSZ Cermet for SOFCs." *International Journal of Hydrogen Energy*, vol. 35, no. 17, 2010, pp. 9440-9447.

[23] Lee, J. -., et al. "Quantitative Analysis of Microstructure and its Related Electrical Property of SOFC Anode, Ni–YSZ Cermet." *Solid State Ionics*, vol. 148, no. 1, 2002, pp. 15-26.

[24] Davarpanah, A., et al. "Ni-YSZ Cermets for Solid Oxide Fuel Cell Anodes Via Two-Step Firing." *International Journal of Hydrogen Energy*, vol. 39, no. 27, 2014, pp. 15046-15056.

[25] Bhattacharyya, S K. An assessment of fuels for nuclear thermal propulsion. United States: N. p., 2002. Web. doi:10.2172/822135.

[26] El-Genk, Mohamed S., and American Institute of Physics. *A Critical Review of Space Nuclear Power and Propulsion, 1984-1993.* AIP Press, American Institute of Physics, New York, 1994.

[27] Haertling, C., and R. J. Hanrahan. "Literature Review of Thermal and Radiation Performance Parameters for High-Temperature, Uranium Dioxide Fueled Cermet Materials." *Journal of Nuclear Materials*, vol. 366, no. 3, 2007, pp. 317-335.

[28] ABABKOV, V. T., "Alloys of the Mo-W System." Metal Science and Heat Treatment, 17, 11, 907-910 (1975)

[29] V.T. ABABKOV and N. N. MORGUNOVA, "Mechanical Properties of Mo-W Alloys," *Metal Science and Heat Treatment*, **15**, *5*, 376-378 (1973)

[30] Marina Sessim & Michael R. Tonks (2021) Multiscale Simulations of Thermal Transport in W-UO_2 CERMET Fuel for Nuclear Thermal Propulsion, Nuclear Technology, 207:7, 1004-1014, DOI: 10.1080/00295450.2021.1910005

[31] Neutron News, Vol. 3, No. 3, 1992, pp. 29-37

[32] American Institute of Aeronautics and Astronautics. (2018). *2018 Joint Propulsion Conference, Cincinnati, Ohio., July 09-11, 2018 - 257.3.2 Spark Plasma Sintering.* American Institute of Aeronautics and Astronautics (AIAA). Retrieved from https://app.knovel.com/hotlink/pdf/id:kt011KF7O1/joint-propulsion-conference/spark-plasma-sintering

[33] Chase, M.W., Jr., NIST-JANAF Themochemical Tables, Fourth Edition, J. Phys. Chem. Ref. Data, Monograph 9, 1998, 1-1951

[34] CRC Handbook of Chemistry and Physics: A Ready-Reference Book of Chemical and Physical Data, 96th Edition. Vol. 2. Beaverton: Ringgold Inc, 2015. ProQuest. 23 Nov. 2021

[35] Chaudri, Khurrum S., et al. "Coupled Analysis for New Fuel Design using UN and UC for SCWR." *Progress in Nuclear Energy (New Series)*, vol. 63, 2013, pp. 57-65.

[36] Shabalin, Igor L., and SpringerLink (Online service). *Ultra-High Temperature Materials I: Carbon (Graphene/Graphite) and Refractory Metals.* Springer Netherlands, Dordrecht, 2014.

[37] Takkunen, Philip D. Fabrication of Cermets of Uranium Nitride and Tungsten or Molybdenum from Mixed Powders and from Coated Particles, https://ntrs.nasa.gov/search.jsp?R=19690012042.

[38] Hirschhorn, J., Hilty, F., Tonks, M.R. *et al.* Review and Preliminary Investigation into Fuel Loss from Cermets Composed of Uranium Nitride and a Molybdenum-Tungsten Alloy for Nuclear Thermal Propulsion Using Mesoscale Simulations. *JOM* (2021). https://doi-org.libproxy.mst.edu/10.1007/s11837-021-04873-x

[39] Ma Benjamín M. “Uranium Nitride, Nitride Fuel.” Nuclear Reactor Materials and Applications, Van Nostrand Reinhold, New York, 1983, pp. 186–198.

[40] Speidel, E O, and Keller, D L. FABRICATION AND PROPERTIES OF HOT-PRESSED URANIUM MONONITRIDE. United States: N. p., 1963. Web. doi:10.2172/4674236.

[41] S N NIKITIN, D P SHORNIKOV, B A TARASOV, V G BARANOV, M A BURLAKOVA. "Imitators of Plutonium and Americium in a Mixed Uranium-Plutonium Nitride Fuel." IOP Conference Series. Materials Science and Engineering, 130, 1, (2016)

[42] R A EVARESTOV, A I PANIN, A V BANDURA AND M V LOSEV "Electronic Structure of Crystalline Uranium Nitrides UN, U2N3 and UN2: LCAO Calculations with the Basis Set Optimization." Journal of Physics. Conference Series, 117, (2008) pp. 012015.

[43] C LOPEZ, X DESCHANELS, C DEN AUWER, J-N CACHIA, S PEUGET, J-M BART. "X-Ray Absorption Studies of Borosilicate Glasses Containing Dissolved Actinides Or Surrogates." Physica Scripta, 2005, (2005)

[44] Toth, Louis, ed. *Transition metal carbides and nitrides*. Elsevier, 2014.

[45] Pierson, Hugh O. Handbook of Refractory Carbides and Nitrides Properties, Characteristics, Processing and Applications. Noyes, 1996.

[46] Török, E., et al. "Young's Modulus of TiN, TiC, ZrN and HfN." Thin Solid Films, vol. 153, no. 1, 1987, pp. 37-43.

[47] KAROL PIETRAK, TOMASZ S. WISNIEWSKI, "A Review of Models for Effective Thermal Conductivity of Composite Materials," *Journal of Power Technologies*, **95**, 14, (2015)

[48] ASTM International. "E1461-13 Standard Test Method for Thermal Diffusivity by the Flash Method." West Conshohocken, PA; ASTM International (2013)

[49] ASTM International. "E228-17 Standard Test Method for Linear Thermal Expansion of Solid Materials With a Push-Rod Dilatometer". West Conshohocken, PA; ASTM International, (2017)

[50] ASTM C1161-13, Standard Test Method for Flexural Strength of Advanced Ceramics at Ambient Temperature, ASTM International, West Conshohocken, PA, 2013, www.astm.org

[51] ASTM C1211-18, Standard Test Method for Flexural Strength of Advanced Ceramics at Elevated Temperatures, ASTM International, West Conshohocken, PA, 2018, www.astm.org

[52] ASTM E1269-11(2018), Standard Test Method for Determining Specific Heat Capacity by Differential Scanning Calorimetry, ASTM International, West Conshohocken, PA, 2018, www.astm.org

[53] Lengauer, Walter, and Alexander Eder. "Nitrides: Transition Metal Solid-State Chemistry." *Encyclopedia of Inorganic Chemistry* (2006).

[54] Warlimont, Hans, and Werner Martienssen. Springer Handbook of Condensed Matter and Materials Data. Springer, New York, 2006.

[55] Podymova, N. B., et al. "Quantitative Evaluation of the Effect of Porosity on the Local Young's Modulus of Isotropic Composites by using the Laser Optoacoustic Method." *Mechanics of Composite Materials*, vol. 49, no. 4, 2013, pp. 411-420.

VITA

James Floyd Mudd was born in Austin, Texas and grew up in Reno, Nevada. He received his B.S. in Material Science & Engineering in May 2020 from University of Nevada, Reno. At the conclusion of that program, he enrolled in the nuclear engineering graduate program at Missouri University of Science and Technology in pursuit of a Master's degree. In May 2022, he received his Master's Degree in Nuclear Engineering from Missouri University of Science and Technology.